

## RESEARCH ARTICLE

# A CloudSat–CALIPSO view of cloud and precipitation in the occluded quadrants of extratropical cyclones

Catherine M. Naud<sup>1</sup>  | Poushali Ghosh<sup>2</sup>  | Jonathan E. Martin<sup>2</sup>  |  
Gregory S. Elsaesser<sup>1</sup>  | Derek J. Posselt<sup>3</sup> 

<sup>1</sup>NASA-GISS, Columbia University,  
New York, New York, USA

<sup>2</sup>Department of Atmospheric and Oceanic  
Sciences, University of  
Wisconsin-Madison, Madison, Wisconsin,  
USA

<sup>3</sup>Jet Propulsion Laboratory, California  
Institute of Technology, Pasadena,  
California, USA

## Correspondence

Catherine M. Naud, NASA-GISS,  
Columbia University, New York, NY, USA.  
Email: [cn2140@columbia.edu](mailto:cn2140@columbia.edu)

## Funding information

Earth Sciences Division  
CloudSat–CALIPSO science team grant,  
Grant/Award Number: 80NSSC20K0085

## Abstract

Using 10 years of satellite-borne radar and lidar observations coupled with a novel method for automated occlusion identification, composite transects of cloud and precipitation across occluded thermal ridges of extratropical cyclones are, for the first time, constructed. These composites confirm that occluded sectors are characterized by the most extensive cloud cover and heaviest precipitation in any of the frontal regions of the cyclone. Hydrometeor frequency in occluded sectors is sensitive to the cyclone's ascent strength but not to the mean precipitable water in the cyclone's environment. This result is in contrast to the strong relationships between hydrometeor frequency and both precipitable water and ascent strength as previously reported in warm frontal regions. In both hemispheres, cloud and precipitation increase with the maximum value of the equivalent potential temperature at 700 hPa within the occluded thermal ridge, until a threshold is reached. For very large values of maximum equivalent potential temperature, hydrometeors become less frequent while precipitation rates increase. It is suggested that this conjunction is a by-product of an increase in the frequency of convection in those instances. While in the Northern Hemisphere occluded sectors exhibit deeper and wider cloud structures than their Southern Hemisphere counterparts, their hydrometeor occurrence frequencies are less. The differences in maximum equivalent potential temperature of the thermal ridges in both hemispheres does not appear to explain the more frequent hydrometeors in the Southern Hemisphere. These relationships offer new perspectives on the interplay between cloud processes and cyclone evolution, as well as new observational constraints for process evaluation of Earth system models.

## KEYWORDS

cloud, CloudSat–CALIPSO, occlusions, precipitation

## 1 | INTRODUCTION

Most of the precipitation in the winter midlatitudes is produced by extratropical cyclones (Hawcroft *et al.*, 2012), whose impacts may also include strong winds, heavy

downpours, blizzards, and cold air outbreaks. While these systems are well understood with regard to their formation, development and eventual dissipation, the role of cloud and precipitation processes in their evolution and potential impact is still the subject of active research.

While such systems are expected to decrease in number as global warming leads to a gradual decline in the equator-to-pole temperature gradient, attendant increases in atmospheric moisture may enhance their vigor via amplification of the developmental impact of latent heating (e.g., Marciano *et al.*, 2015; Michaelis *et al.*, 2017; Zhang & Colle, 2017).

Clouds and precipitation typically form along cold and warm frontal boundaries, where frontogenetically induced ascent and moisture convergence drive the water cycle. Such regions of concentrated latent heat release (LHR) have structural, energetic and developmental impacts on the cyclone as revealed by numerous studies (e.g., Binder *et al.*, 2016; Lackmann, 2002; Sutcliffe & Forsdyke, 1950; Uccellini, 1990). Less organized, isolated convective cells have also been implicated in the production of precipitation in extratropical cyclones (e.g., Binder *et al.*, 2020; Crespo & Posselt, 2016; Oertel *et al.*, 2019; Plummer *et al.*, 2015; Rauber *et al.*, 2015; Rosenow *et al.*, 2014).

Some cyclones entering the post-mature phase of their life cycles undergo the process of occlusion, identified by Bergeron in the context of the Norwegian Cyclone Model and first published in the seminal paper that introduced that model (Bjerknes & Solberg, 1922). Chief among the structural transformations attending the occlusion process is the development of a thermal ridge connecting the cyclone center to the peak of the warm sector where the cold and warm fronts intersect (Martin, 1999a, 1999b; Schultz & Vaughan, 2011, and references therein). Moist air originating in the warm sector boundary layer is forced to ascend cyclonically through this thermal ridge, whose sloping three-dimensional (3-D) manifestation, first described by Crocker *et al.* (1947), was later named the Trough of Warm air Aloft (TROWAL) by Penner (1955). Given that this cyclonically ascending air stream is fed by warm sector boundary layer air and is dynamically forced by wave-scale, not frontal-scale, ascent (Martin, 1999a, 1999b), it is not uncommon to find some of the heaviest precipitation in the storm falling within the so-called occluded sector, poleward and westward of the sea-level pressure minimum (Grim *et al.*, 2007; Han *et al.*, 2007; Martin, 1998b). Consequently, the occluded sector is also a region of substantial, organized LHR. In fact, unlike the companion regions associated with the cold and warm fronts of the cyclone, the LHR in the occluded sector appears to play a critical role in shaping the characteristic occluded thermal structures observed in nature (Posselt & Martin, 2004).

As the planet warms, dependable projections of changes in the frequency, distribution and life cycles of extratropical cyclones are urgently needed. One of the best available tools for glimpsing the nature of a future climate are Earth system models (ESMs) which are becoming

ever more sophisticated. Given the ubiquity of LHR in the cyclone life cycle, accurate representation of moist processes, perhaps especially moist convection, is an important attribute of a reliable ESM. Robust assessments of the projections of such models are tenable when a large volume of trusted observations are at hand for comparison. Ideally, such a set of observations should derive from collections made over multiple years and at multiple locations.

Naud *et al.* (Naud *et al.*, 2012; Naud *et al.*, 2015; Naud, Posselt, & van den Heever, 2018; Schultz, 2018) employed satellite-based radar (onboard CloudSat; Stephens *et al.*, 2002) and lidar (onboard CALIPSO; Winker *et al.*, 2009) profiles, in conjunction with a cyclone data base, to explore the cloud and precipitation distributions associated with objectively identified cold and warm fronts. To date, analysis of the cloud and precipitation distribution in a suitably large sample of occluded sectors has not been undertaken. In Naud *et al.* (2023), we proposed, implemented and tested an automated method that identifies occluded thermal ridges using a gridded 1000:500 hPa thickness product in conjunction with storm positions obtained from a cyclone tracker. In this paper we extend that work to provide an analysis of occluded-sector clouds and precipitation employing observations from CloudSat and CALIPSO.

Launched in 2006, the CloudSat and CALIPSO platforms have collected global vertical profiles of hydrometeors, along with near-surface precipitation estimates, using the unique vantage point of active radar and lidar returns. These measurements are well suited for the foregoing analysis as they allow for reconstruction of the horizontal (along-track) and vertical structure of clouds, and have already been used extensively to explore the 3-D distribution of clouds and precipitation in extratropical cyclones (e.g., Binder *et al.*, 2020; Booth *et al.*, 2013; Govekar *et al.*, 2014; Naud *et al.*, 2010, 2012, 2015). To date, about 11 years of combined radar–lidar observations are available. In this study, we combine observations from CloudSat and CALIPSO with the Naud *et al.* (2023) database of occluded cyclones to construct composites of the vertical distribution of clouds and precipitation across occluded thermal ridges, for all seasons, and both hemispheres. The goal is to provide a decade-long climatology of clouds and precipitation in occluded sectors and explore their sensitivity to environmental characteristics. This climatology can then in turn be used to evaluate numerical models.

The datasets and methodology, in particular for compositing multiple disparate cases, is described in Section 2. The observed distributions of cloud and precipitation across thermal ridges globally are discussed in Section 3, while Section 4 explores the sensitivity of clouds and

precipitation in thermal ridges to various cyclone characteristics. Section 5 reports on observed differences in thermal ridges between the two hemispheres, and finally a summary is presented in Section 6.

## 2 | METHODOLOGY AND DATASETS

The CloudSat and CALIPSO datasets started production in 2006 and flew in close proximity to one another until, in February 2018, the CloudSat platform exited the A-train constellation. Here a joint CloudSat–CALIPSO product is employed that necessitates a short lag between the two observations of the same scene, so we restrict the period of interest to September 2006 through August 2017. During this period CloudSat experienced a battery failure (in 2011) resulting in a lack of data from April 2011 to June 2012. Following the gap in data, CloudSat observations were only collected during daytime hours throughout the 2012–2017 period.

### 2.1 | Identification of occluded quadrants

Naud *et al.* (2023) developed and implemented an automated scheme that identifies the occluded sector of extratropical cyclones. Given that the occluded thermal ridge serves as a two-dimensional (2-D) proxy for the 3-D TROWAL, the essential structural feature of the occluded sector, their method revolves around calculation of the divergence of the unit vector,  $\hat{n}$ , of the 1000:500 hPa thickness field ( $\hat{n} = \frac{\nabla\phi}{|\nabla\phi|}$ ). Areas of convergence of  $\hat{n}$ , with some synoptic adjustment (i.e., multiplying by the magnitude of the gradient of thickness), were shown to consistently identify the location of the TROWAL.

Automating the use of this occluded thermal ridge finding function was also detailed. That process includes several assessments at 6-hr intervals for candidate cyclones, and requires the availability of a cyclone tracking algorithm. First, individual cyclone tracks have to be identified. Then a limited area stretching from  $-10^\circ$  to  $+20^\circ$  longitude and  $\pm 20^\circ$  latitude from the storm center is examined at each 6-hr analysis time. The occlusion-finding-function is then applied within this area, flagging grid points at which the negative divergence (convergence) of  $\hat{n}$  is less than a resolution-dependent threshold. A minimum of eight contiguous grid point neighbors that meet the criterion for identification of a thermal ridge, and whose mean longitude is located to the east of the SLP minimum, represent a qualifying cluster. In order to have identified an occluded extratropical cyclone,

qualifying clusters must at least partially overlap in a cyclone-relative grid for at least two consecutive 6-hr time steps. Finally, if a cluster is identified (1) only once during a cyclone's life cycle, (2) at several non-consecutive 6-hr time steps, or (3) in a consecutive series that ends before the cyclone reaches its peak intensity, that storm and its cluster are not included in the dataset used in any subsequent analyses. These various disqualifications reflect the intentionally conservative nature of the scheme, which is designed to minimize false identification.

### 2.2 | CloudSat and CALIPSO datasets

The CloudSat platform hosts a nadir pointing 94-GHz radar, sensitive to both cloud and light to moderate precipitation down to a reflectivity limit of around  $-30$  dBZ (Stephens *et al.*, 2008). There is no possible distinction between suspended cloud particles and falling hydrometeors in the reflectivity signal. Since the radar is primarily sensitive to larger liquid and ice particles, we will use the term “hydrometeors” to refer to all condensed water that is detected by CloudSat in our analysis. The reflectivity profiles have been processed to identify and report hydrometeor layer locations every 240 m up to the tropopause (Geometrical Profile product, GeoProf, Marchand *et al.*, 2008), in a footprint of 1.4 km across track and 1.7 km along track. For the 2B-GEOPROF–LIDAR product used here (Mace *et al.*, 2009; Mace & Zhang, 2014), the lidar-derived hydrometeor mask (onboard CALIPSO) is also used to supplement the radar, especially for those clouds too tenuous for the radar to identify (thin cirrus or stratus clouds). The resulting product includes the base and top heights of up to five hydrometeor layers. These heights are used to derive a joint hydrometeor mask profile, of 250 m vertical resolution, in each CloudSat footprint.

Precipitation at the surface is also identified in each CloudSat profile and reported in the 2C-PRECIP-COLUMN product (Haynes *et al.*, 2009). These files provide information on whether precipitation might be occurring at the surface, and what phase of precipitation is most probable. In addition, when the lowest 250 m of the profiles contain at least 85% liquid water, a precipitation rate is estimated. Heavy precipitation attenuates the radar return, which minimally affects precipitation identification but does affect the precipitation rate retrieval. This is because the rain rate retrieval relies on the surface backscatter signal, which is obscured in intense-rainfall scenes. The precipitation rate in radar profiles that exhibit complete radar attenuation (no backscatter from Earth's surface) is still reported in the 2C-PRECIP-COLUMN product, but as a negative number. Haynes *et al.* (2009) estimated that this occurs for rainfall rates greater than

$\sim 3\text{--}5\text{ mm}\cdot\text{hr}^{-1}$ . While we elected to use the absolute value of these precipitation estimates to avoid decreasing our sample size (as in Naud, Booth, *et al.*, 2018), we do keep track of the occurrence of radar attenuation in the occluded sectors. Given intense precipitation frequently attenuates the radar signal, especially at the high frequency operated by CloudSat compared to more traditional 3-GHz weather radars, it is acknowledged that the precipitation rate estimates used here may constitute, at times, a significant underestimate.

To help visualize the data used in our analysis, a CloudSat overpass of an occluded thermal ridge observed on December 1, 2006 in the Labrador Sea is portrayed in Figure 1. At 0600 UTC, the cyclone center was located at  $58.25^\circ\text{ N}$  and  $59.21^\circ\text{ W}$ . CloudSat orbit #03158 acquired data across the region within an hour of the cyclone identification, around 0500 UTC, during its descending night-time portion. A moderate-resolution imaging spectroradiometer (MODIS) visible mosaic from around 1600 UTC 1 December 2006 (Figure 1a) sets the broad context. The location of the thermal ridge and the orbit trajectory are shown in Figure 1b. The along-orbit transect of CloudSat reflectivities (Figure 1c) clearly shows two main hydrometeor features: one equatorward of the ridge between  $47^\circ$  and  $50^\circ\text{ N}$ , and the other at the thermal ridge between  $55^\circ$  and  $60^\circ\text{ N}$ . This second feature demonstrates that most of the cloud and precipitation is north of the thermal ridge. In fact, cloud top heights in this second feature (Figure 1d) are up to 10 km some distance north of the ridge. Precipitation rates could be retrieved for the feature south of the ridge over Maritime Canada where most of the precipitation fell as rain, but within the ridge itself both mixed-phase precipitation and snow dominated, making a precipitation rate retrieval impossible (Figure 1e). Though this case was characterized by a nearly perpendicular intersection of the orbit with the occluded thermal ridge axis, most cases in the larger data set do not share this characteristic. Even those that do not, however, still provide valuable information on cloud and precipitation distributions *in the vicinity* of thermal ridges. In the next subsection, a method devised to maximize the number of hydrometeor profile observations incorporated into composites is detailed.

### 2.3 | Constructing composite cross-sections of CloudSat–CALIPSO products

As explained in Naud *et al.* (2023), Modern Era Retrospective analysis for Research and Applications version 2 (MERRA-2; Gelaro *et al.*, 2017) equivalent potential temperature ( $\theta_e$ ) and vertical velocity profiles across all

occluded thermal ridges (OTRs) in our cyclone database were extracted to create composite thermodynamic and kinematic transects across the OTR. This was accomplished by first identifying grid points at which the finding function,  $F$ , was below a prescribed threshold. Such points for the example case from December 2006 are shown as gray crosses in Figure 2a. Next, a regression line in latitude/longitude was calculated through the identified cluster of grid points (labeled “regressed thermal ridge axis” in Figure 2a). At the median longitude of this regression line, a transect is drawn perpendicular to it (labeled “cross-section transect” in Figure 2a). Finally, the regression line was moved along the cross-section transect line until it reached the coincident 700-hPa  $\theta_e$  maximum. The intersection of the transect line and this adjusted regression line was then defined to be the midpoint of a 3000-km long transect along which  $\theta_e$  and  $\omega$  were collected, at 200 km horizontal resolution, up to 15 km above sea level. These  $\theta_e$  and  $\omega$  values were then used to construct the thermodynamic and kinematic composites presented in Naud *et al.* (2023).

Constructing composite cross-sections of the 2B-GEOPROF–LIDAR hydrometeor structure within the identified OTRs involves the challenge of standardizing the derivation of information from satellite profiles taken across a wide range of orientations that individual orbit patterns might take through the OTR. This method is best described using a schematic of a single analysis time, shown in Figure 2 for the previously analyzed 0600 UTC 1 December 2006 occluded identification highlighted in Figure 1. Since the CloudSat–CALIPSO orbit paths traverse the OTR at a multitude of orientations, a variation of the previous compositing methodology is required in each MERRA-2 grid column (gray lines in Figure 2a). The challenge is to collapse the information from a curved cross-section through a 3-D volume onto a line (like the cross-section transect line in Figure 2a), and therefore the following strategy is adopted. First, the precise position of the OTR axis is determined at the degraded resolution of the MERRA-2 data used for the thermal ridge identification (i.e.,  $1.25^\circ \times 1^\circ$ ). Starting at the intersection of the regressed OTR axis (black line in Figure 2a) with each MERRA-2 grid column, the maximum 700-hPa  $\theta_e$  in each grid column is identified and represented by the dots in Figure 2a. The line connecting each of these identifications is the 700-hPa  $\theta_e$  ridge (pink curve in Figure 2a). A set of equidistant lines parallel to the cross-section transect line are drawn within the longitude bounds of the 700-hPa  $\theta_e$  ridge axis to define the *transect area* (red box in Figure 2b). These lines are referred to as “width lines.” Importantly, only the portion of a given orbit path that cuts through the transect area is considered. This restriction facilitates the automated selection of qualifying satellite orbits since any

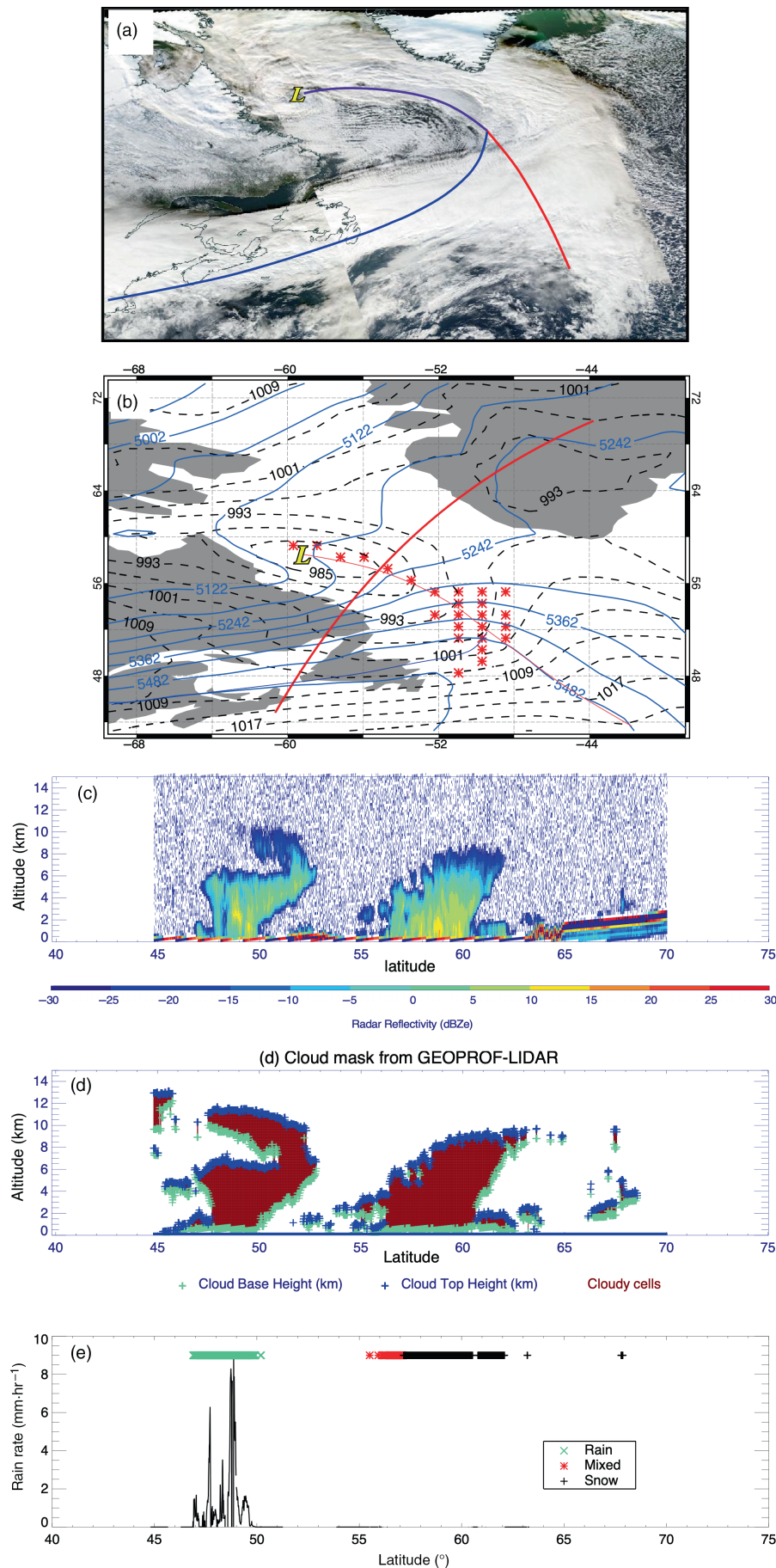


**FIGURE 1** Occluded cyclone in the Labrador Sea on December 1, 2006, with a center at 58.25° N, 59.21° W. (a) Moderate-resolution imaging spectroradiometer (MODIS) visible imagery mosaic from Earth observing system data and information system (EOSDIS) WorldView, Aqua overpass at center at 1550 UTC 1 December 2006. “L” indicates the SLP minimum position while red, blue and purple lines indicate the surface warm, cold and occluded front positions respectively, as determined by 900 hPa vorticity and  $\theta_e$  analysis using modern-era retrospective analysis version 2 (MERRA-2) reanalysis data from 1200 UTC 1 December 2006. (b) SLP (dashed black) and 1000:500 hPa thickness (blue) analysis from MERRA-2 reanalysis valid at 0600 UTC 1 December 2006. SLP is labeled in hPa and contoured every 4 hPa starting at 985 hPa. Thickness is labeled in m and contoured every 60 m starting at 4942 m. Red line marks the CloudSat orbit path through the occluded thermal ridge (OTR) at 0500 UTC 1 December 2006. Red stars mark the location of the thermal ridge; (c) CloudSat reflectivity transect along the orbit between 45° N and 70° N. (d) GEOPROF-LIDAR-derived cloud mask (maroon for “cloudy”), between the cloud base (green) and cloud top (blue) heights from the same orbit path. (e) Along-orbit precipitation type identifications in green for rain, red for mixed phase and black for snow. Solid black line shows rain rates where a retrieval was available.

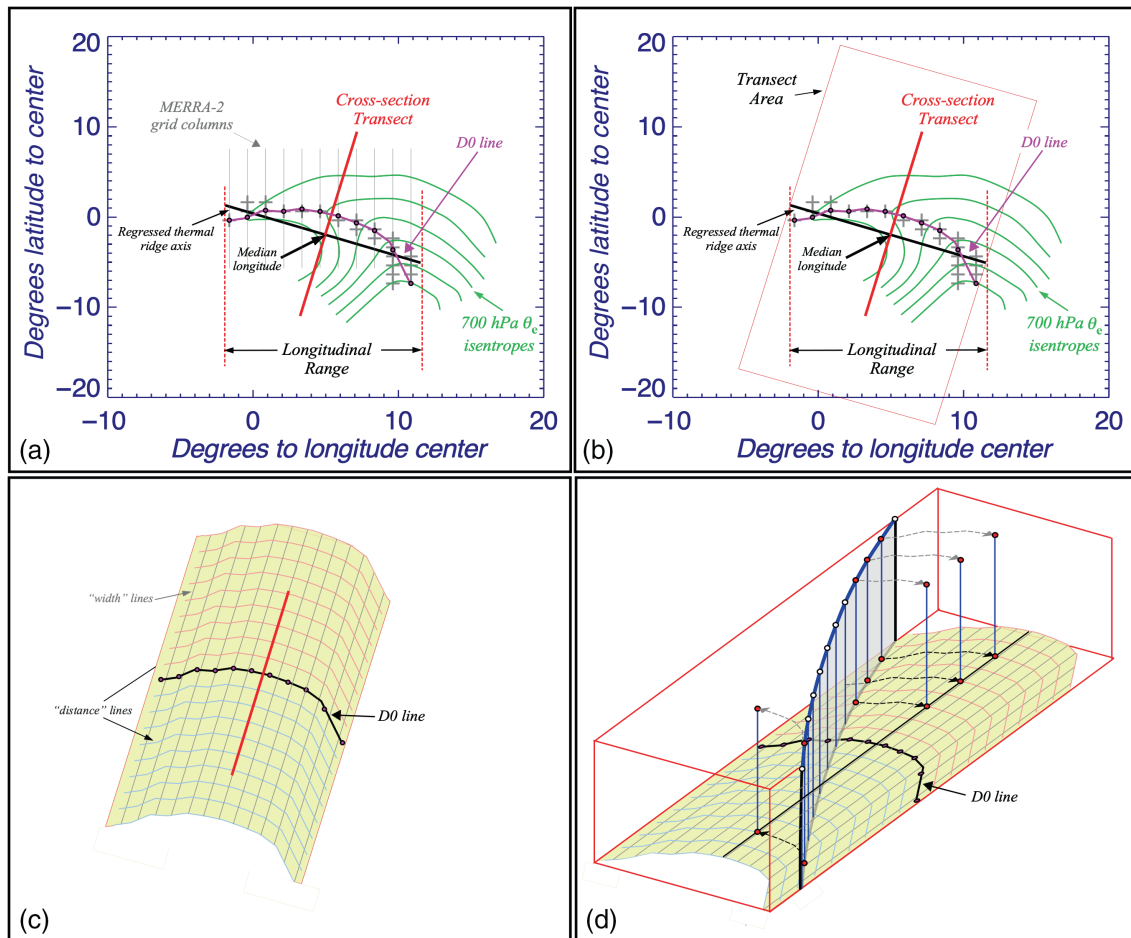


**FIGURE 2** Illustration of the automated method to estimate the distance of each CloudSat profile along the orbit to the occluded thermal ridges (OTRs). The OTR shown is that of an identification on 0600 UTC on 1 December 2006. (a) Green contours show the moist isentropes at 700 hPa, gray + signs indicate the location of the OTR, the black solid its linear regression in longitude–latitude, the pink line (the D0 line) depicting the 700-hPa  $\theta_e$  ridge; gray lines show the modern-era retrospective analysis for research and applications version 2 (MERRA-2) grid columns at each cell. (b) As in (a), with the “Transect Area” surrounding the ridge that is considered for the method in red. (c) Irregular grid of width and distance lines covering the transect area with the pluses corresponding to 100-km increments and colors representing either side of the ridge (blue, cold frontal side; red, warm frontal side). (d) As in (c) but with a schematic vertical CloudSat transect across the “transect area,” with the dashed line showing the projection of each profile onto the transect line.

profile that does not lie within the prescribed area will be disregarded. Along each width line the 700-hPa  $\theta_e$  ridge axis is, by construction, the midpoint of a 3000-km long transect. Together with these width lines, a set of equidistant lines parallel to the 700-hPa  $\theta_e$  ridge axis, referred to as “distance lines” (with the ridge axis denoted as the “D0 line”), form an irregular grid over the transect area (Figure 2c). As illustrated in Figure 2d, it is the distance from the 700-hPa  $\theta_e$  ridge axis, measured along a width line, that determines where the CloudSat–CALIPSO profile information taken at any column on the grid is placed along the composite cross-section line.

Constructing composites of the hydrometeor structure through the OTR requires first determining how many profiles fall within each 100 km distance increment delineated by the distance lines in Figure 2c. The profiles

are organized into a histogram centered on the midpoint of a width line with discrete “distance bins” at each 100-km increment on either side of that midpoint. Using the 250 m hydrometeor mask and representing each of the 250 m thick grid cells as “altitude bins” (Figure 1d), the number of “cloudy” (maroon pluses in Figure 1d) and “clear” cells at various altitudes can be determined for each distance bin. Performing these two steps first facilitates the projection of a 3-D volume of hydrometeor observations from CloudSat–CALIPSO profiles onto a 2-D cross-section along a transect perpendicular to the median grid cell of the OTR. This methodology was applied to CloudSat–CALIPSO orbits traversing the “transect area” in all occluded identifications and the results of the previously described substeps were preserved in preparation for constructing what we refer to as the “grand composite.”

For the grand composite, which uses all identifications, the last step involves dividing the number of “cloudy” cells in each distance and altitude bin by the total number of profiles taken in the respective distance bin. For the surface precipitation products, which are single-valued variables, the same distance-from-thermal ridge method was applied to collect and arrange the data points in the 100-km horizontal resolution grid.

## 2.4 | Verification of the method and sample size impacts

To test the compositing method, we employed MERRA-2  $\theta_e$  profiles in all of the occluded identifications considered by Naud *et al.* (2023). First, we use the Naud *et al.* (2023) method for compositing MERRA-2  $\theta_e$ , that is, profiles collected along the cross-section transect line are composited for all cyclones in the 11-year database as well as for the subset of cyclones that have CloudSat profiles within the “transect area.” The total number of 6-hr cyclone snapshots for which the latter condition is met is 4828 out of the 27,240 occluded identifications in our database (all seasons, both hemispheres). Note that contrary to CloudSat–CALIPSO hydrometeor profiles that are available every 1.4 km, MERRA-2  $0.625^\circ \times 0.5^\circ$  spatial

resolution is rather coarse, so for MERRA-2  $\theta_e$  transects we keep the original 200-km horizontal resolution instead of 100 km as used for the observations. The composite transect of MERRA-2  $\theta_e$  across the ridges for the cyclones in the CloudSat subset faithfully reproduces the canonical thermal structure of the occlusion (Figure 3a) and, in fact, is virtually identical to the composite obtained for all occlusion identifications with most differences being less than 1 K (Figure 3b). This test confirms that (1) the subset of cyclones viewed by CloudSat exhibits no bias compared to the overall population with respect to the structure of the OTR, (2) the missing months in the data are not a source of bias either, and (3) the smaller population size of CloudSat-observed identifications does not affect the results. In short, the distribution of cyclones observed with CloudSat are collectively representative of all occluded cyclones.

Next the impact on the composite  $\theta_e$  structure of the CloudSat–CALIPSO orbit paths traversing the OTR at a variety of orientations was tested. For this, MERRA-2 profiles were collected *along the CloudSat orbits only*, using a simple nearest neighbor approach, and then the method illustrated in Figure 2 was followed to construct the  $\theta_e$  composite. The composite transect thus obtained is shown in Figure 3c. Though it is not identical to, nor as smooth as, that obtained using the Naud *et al.* (2023) method,

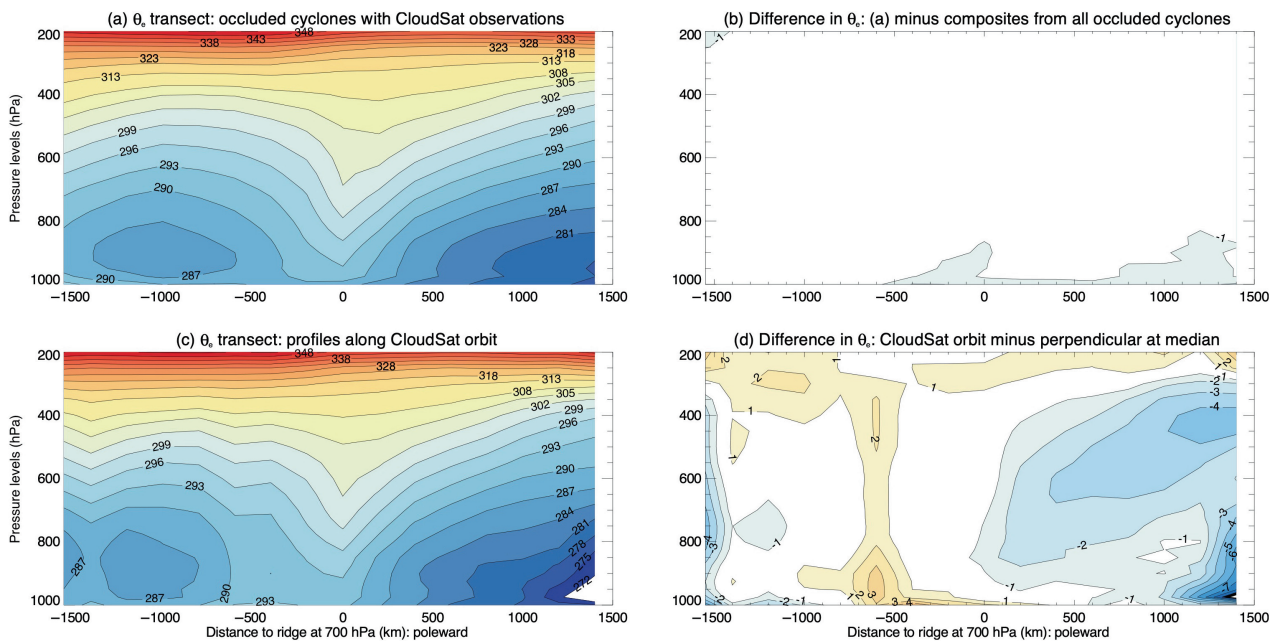


**FIGURE 3** (a) Composite transect of modern-era retrospective analysis for research and applications version 2 (MERRA-2)  $\theta_e$  across occluded thermal ridges (OTRs) with CloudSat orbits within the vicinity of the thermal ridge in the Northern Hemisphere (NH) winter between 2006 and 2017 constructed as in Naud *et al.* (2023).  $\theta_e$  is labeled in K and contoured every 3 K starting at 272 K. (b) Difference between the composite shown in (a) and the composite obtained for all NH winter occluded cyclones. (c)  $\theta_e$  transect obtained along the Cloudsat orbit using the “nearest-neighbor” method described in the text. (d) Difference between the composite shown in (c) and that shown in (a). The difference in  $\theta_e$  is contoured every 1 K, starting at  $-7$  K.

especially on the equatorward side of the thermal ridge, it does capture the same occluded thermal characteristics with most differences within 4 K in absolute value (Figure 3d). Importantly, the differences in  $\theta_e$  are small at the location of the ridge itself (zero point along the x-axis). These tests demonstrate that the CloudSat sampling technique described in this section does not introduce an unreasonable bias to the composite transect. Given that the compositing method performs well, confident exploration of the cloud and precipitation composite transects is presented next.

### 3 | CLOUD AND PRECIPITATION DISTRIBUTIONS ACROSS THE OCCLUDED THERMAL RIDGE

As mentioned in Section 2, the present study employs observations from the period September 2006 to August

2017. In this section the composite hydrometeor distribution across all thermal ridges in the database of occlusions with a CloudSat overpass is presented along with the corresponding distribution of surface precipitation.

#### 3.1 | Hydrometeor distribution across OTRs: Comparison with warm and cold front intersects

With CloudSat–CALIPSO hydrometeor mask profiles, a composite transect of hydrometeor frequency of occurrence across all OTRs identified between September 2006 and August 2017 in both hemispheres was constructed (Figure 4a). Southern (SH) and Northern Hemisphere (NH) transects were each constructed such that the x-axis is directed poleward from left to right with  $x=0$  marking, as previously described, the composite position of the 700-hPa  $\theta_e$  maximum in the OTR. Importantly, the

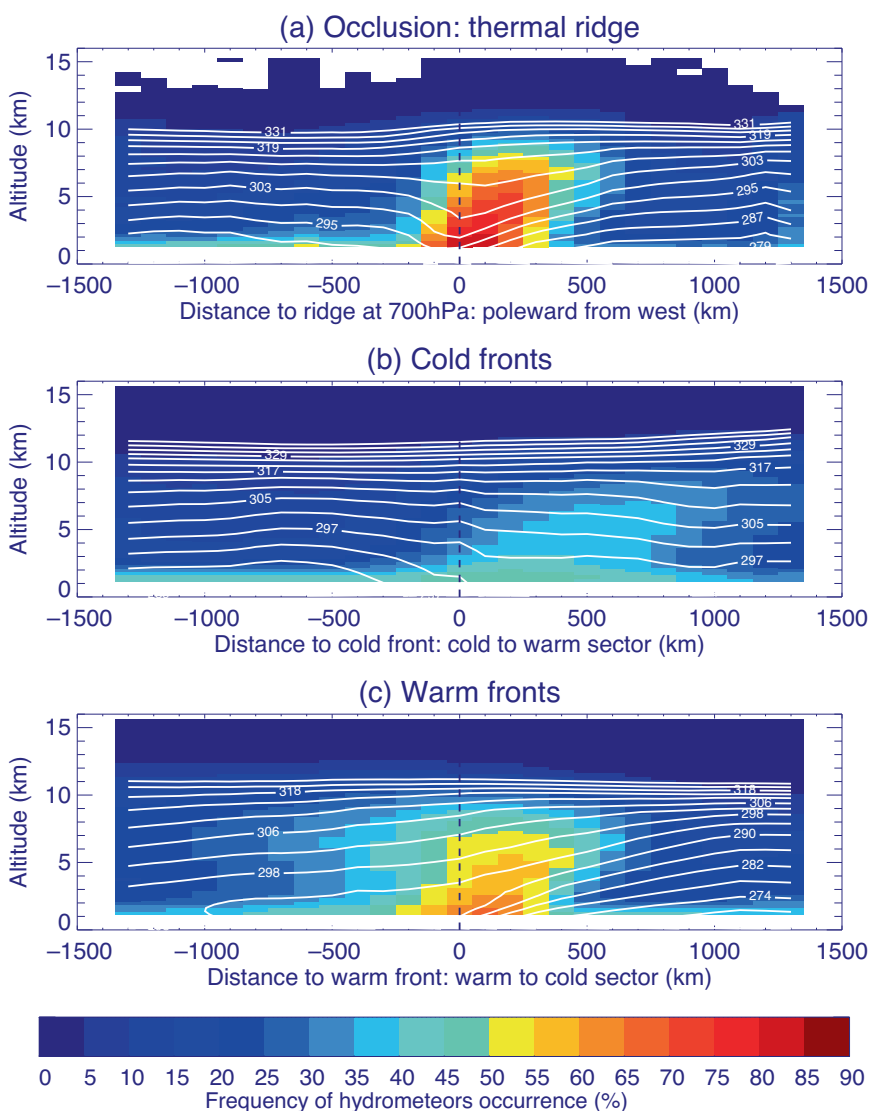


**FIGURE 4** Composite transects of CloudSat–CALIPSO derived hydrometeor frequency of occurrence (in %, colored contours every 5%) across (a) thermal ridges in occluded sectors, (b) cold fronts and (c) warm fronts. In each panel, the vertical dashed line indicates the location of (a) the thermal ridge at 700 hPa, (b) the cold front at 850 hPa and (c) the warm front at 1 km above the surface. The solid contours indicate the composite of equivalent potential temperature from modern-era retrospective analysis for research and applications version 2 (MERRA-2) in K, every 4 K.

surface-occluded front is located where the sloping axis of maximum  $\theta_e$  intersects the ground. In each of the composites in Naud *et al.* (2023) (see their figures 11 and 15), this feature is approx. 100–200 km equatorward of  $x=0$ . The hydrometeor distribution across the thermal ridge increases with altitude poleward of the ridge, with frequencies greater than 50% up to an altitude of 8 and 500 km poleward of  $x=0$ . The composited hydrometeor distribution is consistent with the distribution of both  $\theta_e$  (also shown) and strong vertical velocity characterizing the occluded thermal ridge (cf. Naud *et al.*, 2023). This coincidence confirms that the maximum hydrometeor frequency in the occluded sector is more closely related to the TROWAL position than to the surface-occluded front.

Using the same CloudSat–CALIPSO dataset, Naud *et al.* (2015, 2016) and Naud, Posselt, and van den Heever (2018) constructed cold front transects and Naud *et al.* (2010, 2012) constructed similar composites across warm fronts. The cold fronts were identified at 850 hPa using a combination of the thermal gradient method of Hewson (1998) applied to MERRA-2 potential temperatures and the wind direction change method of Simmonds *et al.* (2012) also applied to MERRA-2 winds. The warm fronts were obtained using the Hewson (1998) method applied to MERRA-2 potential temperatures at 1 km above mean sea level. Taking advantage of the objective identification of occlusions afforded by the method of Naud *et al.* (2023), these prior results have been modified by removing all occluded cyclones that had previously been erroneously included in the cold and warm frontal composites. The revised hydrometeor frequency of occurrence composites across cold and warm fronts, in both hemispheres for the same 2006–2017 period, are shown in Figure 4b and c respectively. Figure 4 demonstrates that the frequency of hydrometeor occurrence across the occluded sectors is quite different from that in either the cold or warm front composites.

Composites, by construction, are designed to reveal the most salient features of a collection of often disparate cases. As such, they are not meant to look like any of the individual cases that constitute them. Thus, if the frequency of hydrometeor occurrence in a given composite is low, it does not necessarily imply that there are few clouds associated with the feature in question. Instead, it may reveal that there is significant variability in cloud location within the area that is sampled, as well as across the multiple cases that contribute to the composite. In cold frontal regions, clouds are often found in localized, sometimes discontinuous bands of various widths, which can be found in a large variety of locations with respect to the front itself. This causes the accumulated frequency of hydrometeor occurrence across cold fronts to appear to be relatively low as compared to warm frontal or occluded

thermal ridge regions. Such spatial variability is smaller in warm frontal regions where cloud and precipitation formation is more systematically tied to ascent and moisture transport associated with the warm conveyor belt. Variability in the composite is present, however, because (1) the observations sense systems in various stages of the cyclone's lifecycle, (2) warm fronts vary in length and, (3) warm fronts can be rather cloud-free toward their eastern extremity. In contrast, the greater frequency of hydrometeor occurrence across OTRs is a function of both the limited geographical extent of the TROWAL as well as the nature of the ascent that characterizes it. The warm frontal ascent arises in response to frontogenetical forcing, and is manifest as transverse couplets that straddle the vertical shear. On the other hand, the ascent in the occluded sector is fueled by positive vorticity advection by the thermal wind (Sutcliffe, 1947), a robust, wave-scale forcing for ascent that also makes a primary contribution to mid-latitude development (Martin, 1999a, 1999b, 2006). As a result, hydrometeor frequencies are much larger in occluded sectors than they are in warm frontal regions.

### 3.2 | Precipitation across the OTR

Using the CloudSat product that provides information on whether or not surface precipitation is occurring, and what thermodynamic phase dominates, we next examine the composite transect of precipitation occurrence across the thermal ridge (Figure 5a). Consistent with the hydrometeor distribution, surface precipitation occurs up to 80% of the time within the thermal ridge, with the maximum shifted poleward from the location of the 700-hPa  $\theta_e$  ridge axis. Again, the bulk of the precipitation is associated with the TROWAL and not with the surface-occluded front. In contrast, on the equator/cold front side of the ridge, precipitation occurs up to 40% of the time while it drops to 20% at approximately 500 km poleward of the TROWAL region. Focusing now on the thermodynamic phase of the precipitation, Figure 5a indicates that liquid precipitation peaks slightly equatorward of the ridge, and reaches a frequency of occurrence close to 25%; the mixed phase peaks in the first 100 km poleward of the 700-hPa  $\theta_e$  ridge and is more frequent at 30%, while the snow fraction also peaks at 30% but more clearly on the polar side of the ridge at  $\sim 100$  km. While the three phases are nearly equally represented on the equatorward side of the ridge, not surprisingly rain frequency drops off more rapidly on the polar side than the other two phases, and snow tends to flatten out beyond 500 km poleward at around 15% frequency.

Precipitation rates can only be retrieved if the near-surface precipitation is at least 85% liquid. On the equatorward side of the ridge this condition is met at least

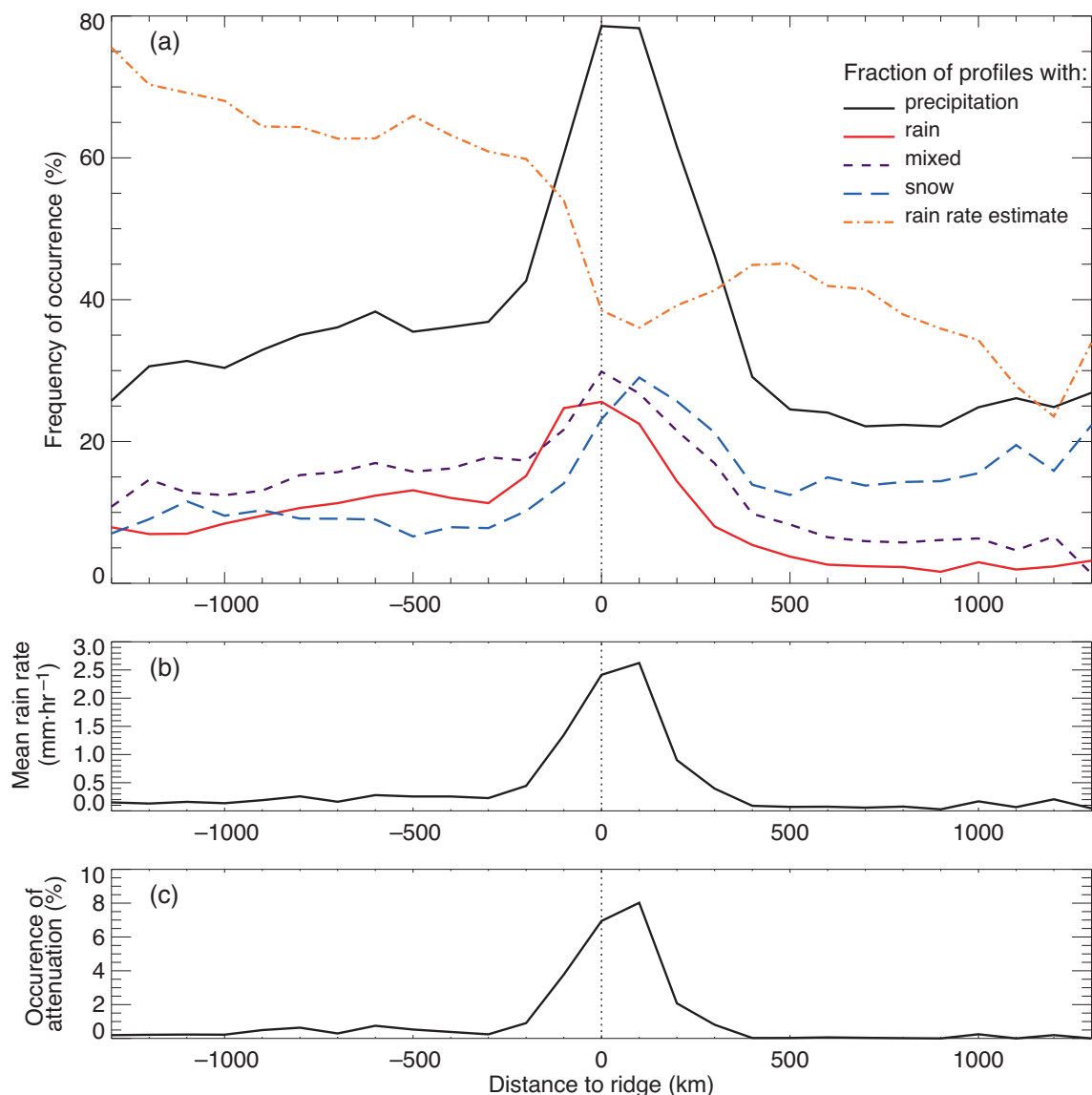


**FIGURE 5** Composite transect across thermal ridges of (a) the frequency of occurrence of precipitation (solid black), of liquid precipitation or rain (red dot-dot-dot-dash), of mixed liquid/solid precipitation (purple dash), of solid precipitation or snow (blue long dash) and of the availability of a precipitation rate estimate (orange dot-dash), (b) of the precipitation rate (in  $\text{mm}\cdot\text{hr}^{-1}$ ) when estimated and (c) the frequency of occurrence of attenuated profiles (in %). The vertical dotted line in all three panels indicates the location of the thermal ridge at 700 hPa.

60% of the time to about  $-200$  km (Figure 5a). It then drops down to 35% of the time at  $+100$  km poleward of the ridge. With this caveat in mind, the mean rain rates are composited across the thermal ridge (Figure 5b). The average includes profiles for which the retrieval algorithm determined that no precipitation reached the ground (i.e., all profiles with rate  $R \geq 0 \text{ mm}\cdot\text{hr}^{-1}$  are included). In accordance with the cloud and precipitation distributions, the rate increases sharply from 200 km equatorward of the 700-hPa  $\theta_e$  ridge poleward and reaches a maximum of  $2.5 \text{ mm}\cdot\text{hr}^{-1}$  at  $+100$  km before dropping rapidly to  $0.5 \text{ mm}\cdot\text{hr}^{-1}$  at  $+300$  km poleward. This maximum in precipitation rate is significantly larger than what

is typically found in cold frontal regions composites ( $0.3 \text{ mm}\cdot\text{hr}^{-1}$ , Naud *et al.*, 2015, their Figure 5), or in SH warm frontal zones ( $\sim 1.8 \text{ mm}\cdot\text{hr}^{-1}$ , Naud *et al.*, 2012; their Figure 11). In fact, only for a subset of NH cyclones at their peak intensity are the mean precipitation rates in warm frontal zones comparable to the occluded sector mean presented here (cf. Naud *et al.*, 2012). Again, this is likely related to the much lower hydrometeor frequency variability in OTRs compared to cold or warm frontal regions. Finally, as a means of confirming how intense precipitation might be in the TROWAL region, Figure 5c shows that the frequency of radar attenuation increases rapidly from near 0% at 300 km equatorward of the 700-hPa  $\theta_e$  ridge to

8% of the time 200 km poleward. This not only confirms that precipitation can be intense in the ridge area, but also serves to caution that in the more extreme cases the radar return can be fully attenuated, and therefore the mean precipitation rate provided here can be underestimated.

Our results provide the first global climatological picture of condensate distributions in oceanic OTRs. Given the prevalence of both cloud and precipitation within and across disparate OTRs, we next explore the large-scale factors that affect and modulate cloud and precipitation frequency.

#### 4 | SENSITIVITY OF CLOUD AND PRECIPITATION TO THE CHARACTERISTICS OF THE OCCLUDED CYCLONE

As summarized earlier, moist air originating in the warm sector boundary layer is forced to ascend cyclonically through the OTR and anticyclonically across the warm front. However, the TROWAL air stream is dynamically forced by wave-scale, not frontal-scale, ascent (Martin, 1999a, 1999b). Previous studies have demonstrated that cloud extent and precipitation in cyclones are strongly dependent on the vigor of the cyclone as well as how much precipitable water is available (e.g., Field & Wood, 2007). Such a connection was clearly demonstrated for warm frontal regions using wind speeds (Field & Wood, 2007) and both cold and warm frontal regions using ascent strength (Naud *et al.*, 2017). Therefore we examine whether hydrometeor frequencies in the OTRs show more compelling sensitivities to ascent strength and mean cyclone precipitable water (PW) (as is the case for warm frontal regions), or to a more thermal-ridge-specific metric, the equivalent potential temperature along the thermal ridge.

##### 4.1 | Sensitivity to mean cyclone precipitable water and ascent strength

Assessment of a relationship between ascent strength and hydrometeor distribution was afforded by calculating the mean 500-hPa ascent from MERRA-2 within a 1500-km radius of the surface cyclone center for each occluded identification that had a corresponding satellite transect. For the same events, the MERRA-2 PW within the same radius for each identification was also averaged. Next, the analysis partitioned all such occluded identifications (from both hemispheres and all seasons) into three equally-sized PW categories and three equally-sized ascent strength categories. The resulting PW thresholds were 6

**TABLE 1** Number of thermal ridges per each precipitable water (PW)-ascent strength category defined using the entire (both hemispheres, all seasons) dataset.

	$-6 \text{ hPa}\cdot\text{hr}^{-1}$ < ascent	$-8 \text{ hPa}\cdot\text{hr}^{-1}$ < ascent < $-6 \text{ hPa}\cdot\text{hr}^{-1}$	Ascent < $-8 \text{ hPa}\cdot\text{hr}^{-1}$
PW < 6 mm	649	426	290
6 < PW < 9 mm	415	500	451
9 mm < PW	303	440	624

*Note:* When sorting the dataset based on mean cyclone-wide PW, three equal-size subsets are found for thresholds PW = 6 mm, and PW = 9 mm. When sorting based on mean ascent strength,  $-6$  and  $-8 \text{ hPa}\cdot\text{hr}^{-1}$  provide three equal-size subsets.

and 9 mm while the ascent strength thresholds were  $-6$  and  $-8 \text{ hPa}\cdot\text{hr}^{-1}$ . Partitioning into three categories provides nine distinct elements in a  $3 \times 3$  matrix of ascent strength and PW. The number of OTRs per element is provided in Table 1. Not surprisingly the number of cases per element varies. Occluded identifications in drier environments are preferentially associated with weak ascent, while progressively moister environments are characterized by stronger ascent.

The resulting analysis of hydrometeor distribution in OTRs as a function of both PW and ascent strength is quite intriguing (Figure 6). In all three PW categories increasing ascent strength appears to increase both the vertical and poleward extents of the hydrometeors in the OTR. For the low and medium PW categories (top two rows of Figure 6) there is also a tendency for the maxima in hydrometeor frequencies (in excess of 75%) to increase with increasing ascent strength. However, for the largest PW category (Figure 6c,f,i), hydrometeor maximum frequency does not change with increasing ascent strength. In addition, there appears to be no evidence of a relationship between hydrometeor frequency of occurrence and environmental PW (i.e., consider the *columns* in Figure 6). In contrast, using the same PW-ascent strength categories, hydrometeor transects across warm fronts show a clear dependence of hydrometeor frequency of occurrence distribution on both PW (impact on width) and ascent strength (impact on vertical extent) (Figure 7). Given that the moisture processed by both the warm frontal and thermal ridge regions originates in the warm sector (where PW is often a maximum), this result lends additional observational support to the evolving notion that cloud processes in OTRs are not driven by the same physical factors that operate in warm frontal regions. To help better understand processes potentially unique to the occluded sector, we next examine the impact of using the equivalent potential temperature along the ridge as a means to classify the occluded cyclones.

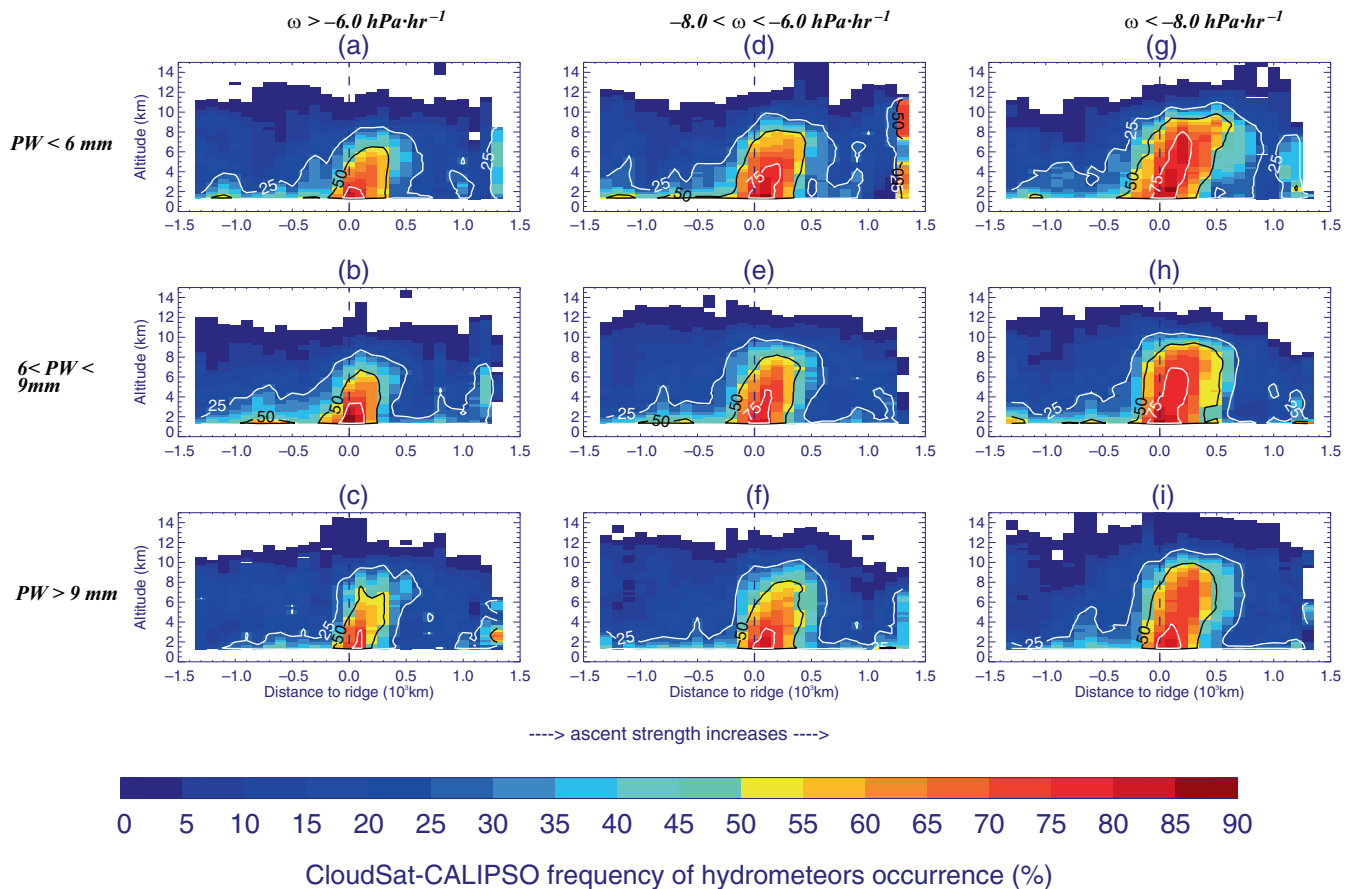


**FIGURE 6** Composite transects of hydrometeor frequency of occurrence across thermal ridges for three precipitable water (PW) categories (top to bottom and three ascent strength categories (left to right): (a, d, g)  $PW < 6 \text{ mm}$ ; (b, e, h)  $6 < PW < 9 \text{ mm}$ ; and (c, f, i)  $PW > 9 \text{ mm}$ . (a, b, c) Ascent strength  $> -6 \text{ hPa}\cdot\text{hr}^{-1}$ , (d, e, f)  $-8 < \text{ascent strength} < -6 \text{ hPa}\cdot\text{hr}^{-1}$ , and (g, h, i) ascent strength  $< -8 \text{ hPa}\cdot\text{hr}^{-1}$ . The vertical dashed line indicates the location of the thermal ridge at 700 hPa.

## 4.2 | Sensitivity to the $\theta_e$ maximum in the occluded thermal ridge

In Naud *et al.* (2023), the thermal and kinematic structure of the thermal ridge was considered as a function of the maximum in  $\theta_e$  at 700 hPa for both NH and SH winter cyclones. A clear relationship emerged wherein lower  $\theta_e$ -occluded identifications were found to exhibit shallower and more upright thermal structures, as well as weaker vertical motions, than their higher  $\theta_e$  counterparts, implying stronger latent heat release in the latter identifications. In this section we examine what these differences imply for cloud and precipitation distributions across OTRs in both hemispheres and all seasons.

Because the number of occluded identifications with cloud observations is substantially smaller than the set of all occluded identifications considered by Naud *et al.* (2023), the present analysis divides the population of the former set (i.e., all seasons, both hemispheres) into three categories of  $\theta_e$  (instead of the six employed

in Naud *et al.*, 2023). To define the categories, we sort the identifications from the lowest to highest 700-hPa  $\theta_e$  value at the axis of the ridge, and divide the whole population into terciles. As in Naud *et al.* (2023), the subset of cyclones selected here peaks in the range 285–305 K, with NH ridges overall warmer than their SH counterparts (Figure 8). The three  $\theta_e$  categories obtained from the full set (both hemispheres, all seasons) are:  $\theta_e < 293 \text{ K}$ ,  $293 \text{ K} < \theta_e < 304 \text{ K}$  and  $\theta_e > 304 \text{ K}$ .

Over the global oceans, hydrometeor frequency of occurrence in OTRs expands upward and poleward from the low to high  $\theta_e$  terciles (Figure 9), and is consistent with the mean  $\theta_e$  transects (Figure 9a–c): the lowest  $\theta_e$  cases are shallower than the “warmer” cases, while the highest  $\theta_e$  cases exhibit a more pronounced poleward tilt than the “cooler” cases. Focusing more specifically on the region with hydrometeor occurrence greater than 50%, the poleward expansion as a function of increasing  $\theta_e$  is clear (Figure 10), but surprisingly, at the 75% level area, the warmest cases show a drop in maximum frequency compared to medium  $\theta_e$  cases. This suggests that

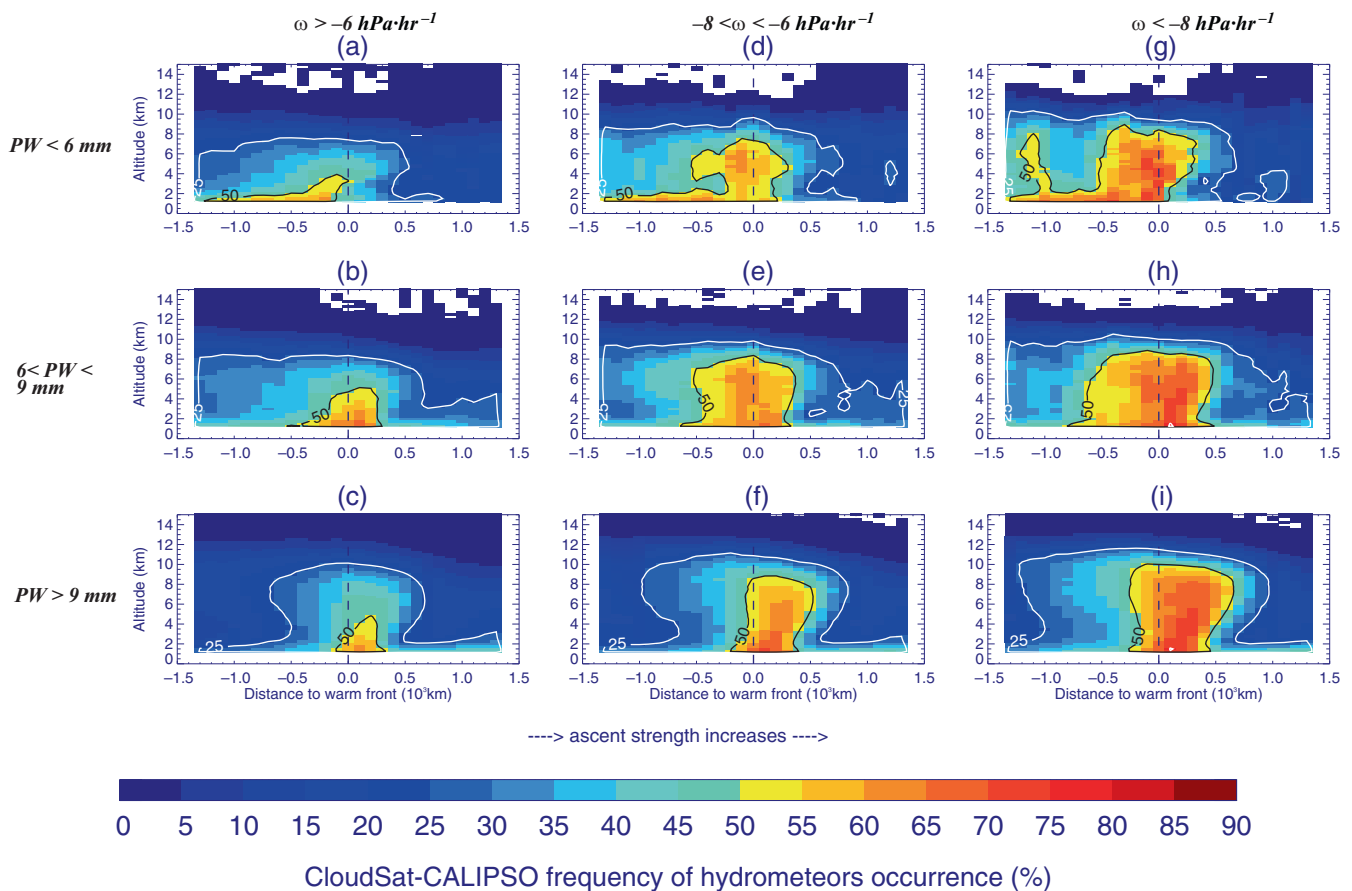


**FIGURE 7** Composite transects of hydrometeor frequency of occurrence across warm fronts for three precipitable water (PW) categories (top to bottom and three ascent strength categories (left to right): (a, d, g)  $PW < 6$  mm; (b, e, h)  $6 < PW < 9$  mm; and (c, f, i)  $PW > 9$  mm. (a, b, c) Ascent strength  $> -6$  hPa·hr $^{-1}$ ; (d, e, f)  $-6 < \text{ascent strength} < -8$  hPa·hr $^{-1}$ ; and (g, h, i) ascent strength  $< -8$  hPa·hr $^{-1}$ . The vertical dashed line indicates the location of the warm front at 1 km above the surface. Adapted from Figure 11 in Naud *et al.* (2017) to include both Northern-Hemisphere and Southern Hemisphere warm fronts and exclude occluded cyclones, as well as use the same PW-ascent strength categories as in Figure 6.

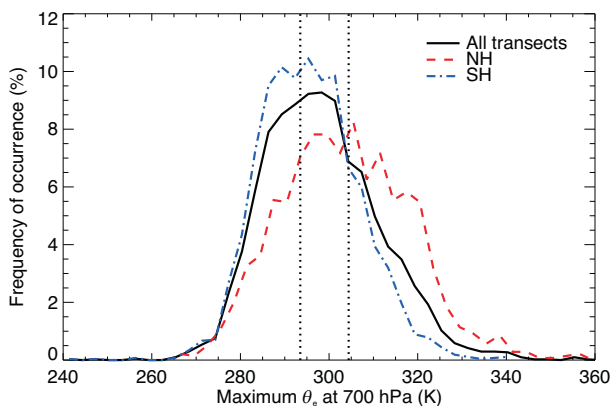


**FIGURE 8** Distribution of the maximum of  $\theta_e$  at 700 hPa in the thermal ridge for all cyclones — both hemispheres, all seasons—with CloudSat–CALIPSO observations (solid), those in the Northern Hemisphere (NH) (dashed red) and in the Southern Hemisphere (SH) (dot-dash blue). The two dotted lines indicate the  $\theta_e$  values that separate the entire (both hemispheres) population of cyclones into three equally sized subsets.

hydrometeors occur over a wider area in the warmest ridges, but are less concentrated in them. Because the difference in maximum frequency occurs at low altitude, there is a possibility that this is caused by a change in precipitation frequency: CloudSat reflectivity profiles do not have information enabling a straightforward distinction between suspended and falling condensate in regions where both cloud and precipitation can occur. However, the frequency of occurrence of precipitation at the surface is very similar across the three  $\theta_e$  categories, with differences of the order of only a few percent (Figure 11a). That said, the difference in mean precipitation rate is more significant (Figure 11b) and suggests more efficient precipitation production in the warmest  $\theta_e$  category. This is somewhat corroborated by the distinct peak in saturation occurrence for the warmest category compared to either of the lower  $\theta_e$  categories (Figure 11c). All three measures suggest more precipitation in the warmest  $\theta_e$  category than in the coldest and therefore the contrast in hydrometeor

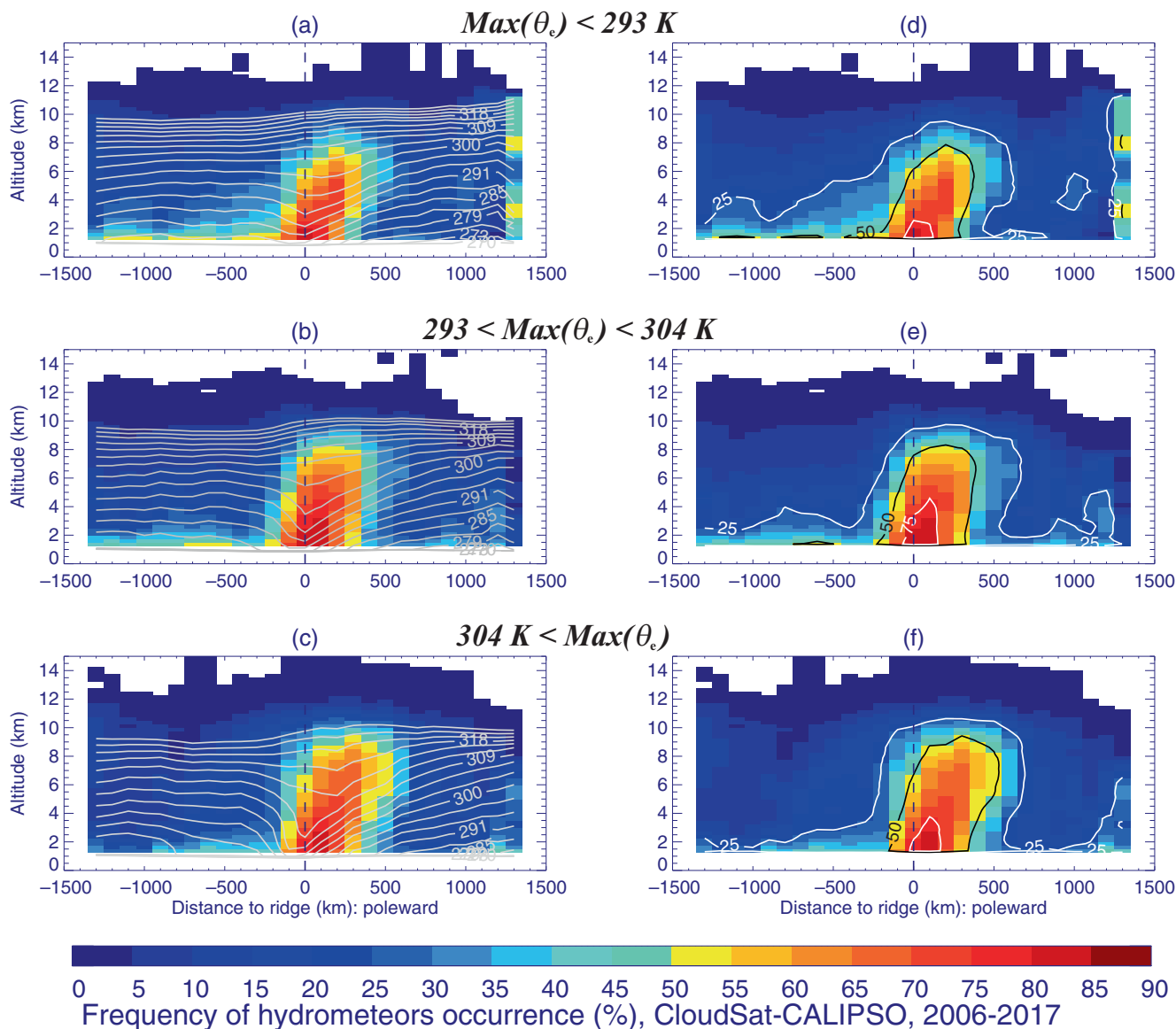


**FIGURE 9** Composite transect of hydrometeor frequency of occurrence for occluded thermal ridges (OTRs) classified based on the maximum  $\theta_e$  at 700 hPa: (a, d)  $\max(\theta_e) < 293$  K; (b, e)  $293 \text{ K} < \max(\theta_e) < 304$  K; and (c, f)  $304 \text{ K} < \max(\theta_e)$ . Frequency of occurrence is shaded every 5% from 0% to 90%.  $\theta_e$  contours (white solid lines) labeled in K and contoured every 3 K in (a–c). Thin solid lines are 25%, 50%, and 75% frequency level contours in (d–f). The vertical line indicates the location of the ridge at 700 hPa.

frequency maximum is not caused by a reduction in precipitation at low altitudes. Instead, it is suggested that convection occurs more often in the warmest category, which would be consistent with its attendant more scattered clouds and larger precipitation rates. Without additional information, however, this suggestion cannot be verified.

Despite the lack of cloud and precipitation variability in OTRs and the seeming lack of any connection to PW, some differences between hemispheres may yet exist. In the next section we separately consider northern and SH systems in order to identify any such differences.

## 5 | COMPARISON BETWEEN NORTHERN- AND SOUTHERN-HEMISPHERE OCCLUDED THERMAL RIDGES

Given the hemispheric differences in the thermodynamic and kinematic composites of occluded sectors detailed in Naud *et al.* (2023), a similar stratification of the cloud and precipitation distributions by hemisphere is undertaken here. Naud *et al.* (2023) found that SH occlusions tend to occur year-round with a frequency peak in the fall, while in the NH the seasonality is much more robust with very few occlusions in the summer and a clear maximum in the

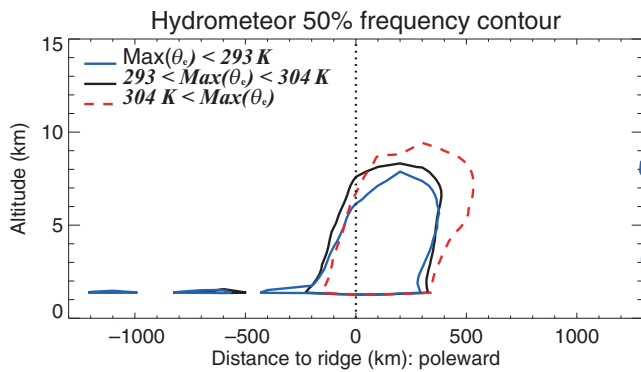


**FIGURE 10** The location of the hydrometeor 50% frequency contour as a function of altitude and distance to the thermal ridge at 700 hPa for occluded cyclones with a maximum value of  $\theta_e$  at 700 hPa along the ridge of less than 293 K (blue; dot-dot-dot-dash), between 293 and 304 K (black; solid) and greater than 304 K (red; dashed). The vertical dotted line indicates the location of the ridge at 700 hPa.

winter. Also, NH occlusions occur over a wider range of latitudes, while very few SH occluded systems occur north (equatorward) of 40° S. These geographic specificities likely condition the environment within occluded cyclones and so different average cloud and precipitation distributions might be expected between the two hemispheres.

## 5.1 | Northern and Southern Hemisphere occluded thermal ridges

With respect to hydrometeor transects in each hemisphere (Figure 12), while there are no evident differences between the two hemispheres, there are some subtle features that are worth noting. First the NH hydrometeor distribution (Figure 12a) appears to extend to higher altitudes (Figure 12c). Second, the region of frequencies in excess of 50% appears to be more horizontally restricted

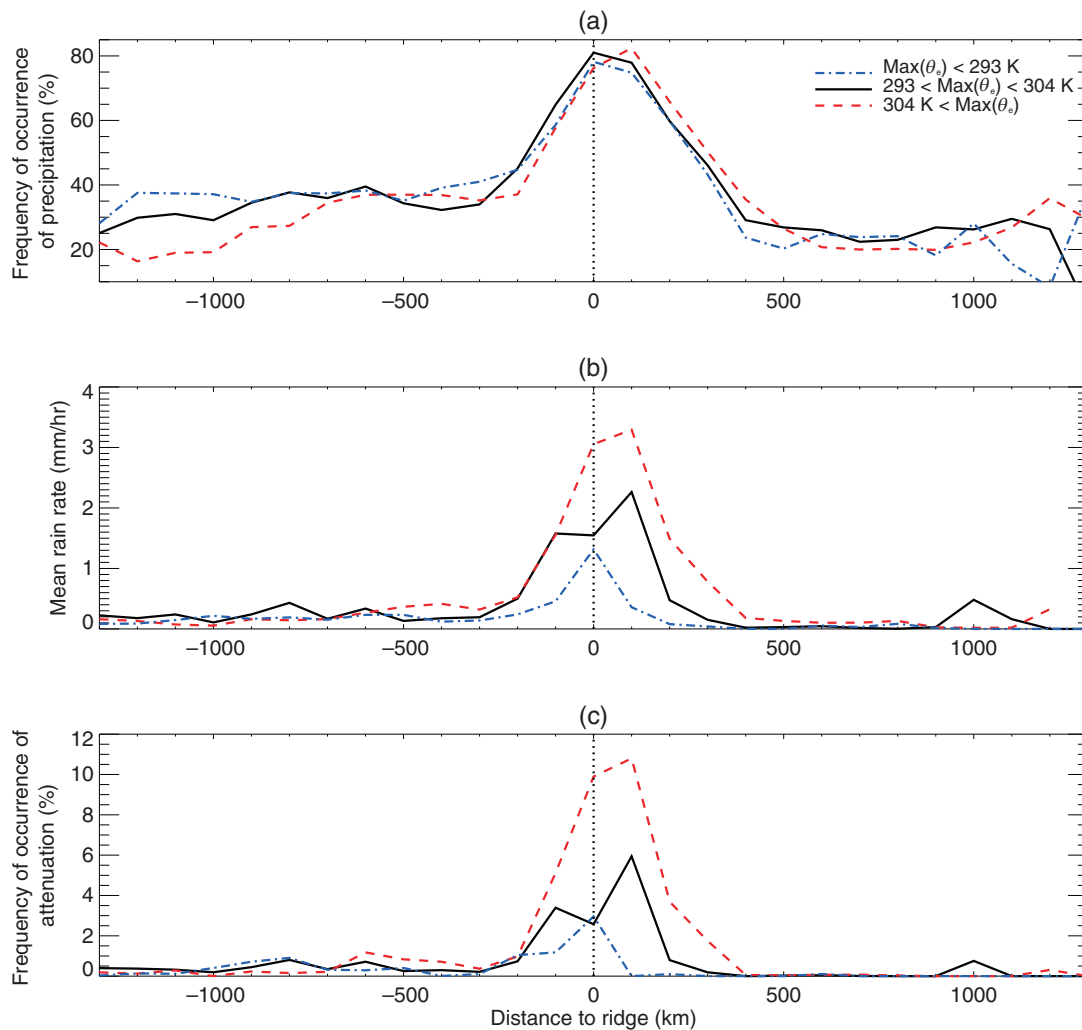


**FIGURE 11** Composite transect across thermal ridges of (a) frequency of occurrence of precipitation (%); (b) mean rain rate ( $\text{mm}\cdot\text{hr}^{-1}$ ); and (c) occurrence of attenuation (%) for occluded thermal ridges (OTRs) with  $\theta_e < 293$  K (blue dot-dash);  $293 \text{ K} < \theta_e < 304$  K (red dashed); and  $304 \text{ K} < \theta_e$  (black solid). The vertical dotted line in all three panels indicates the location of the thermal ridge at 700 hPa.

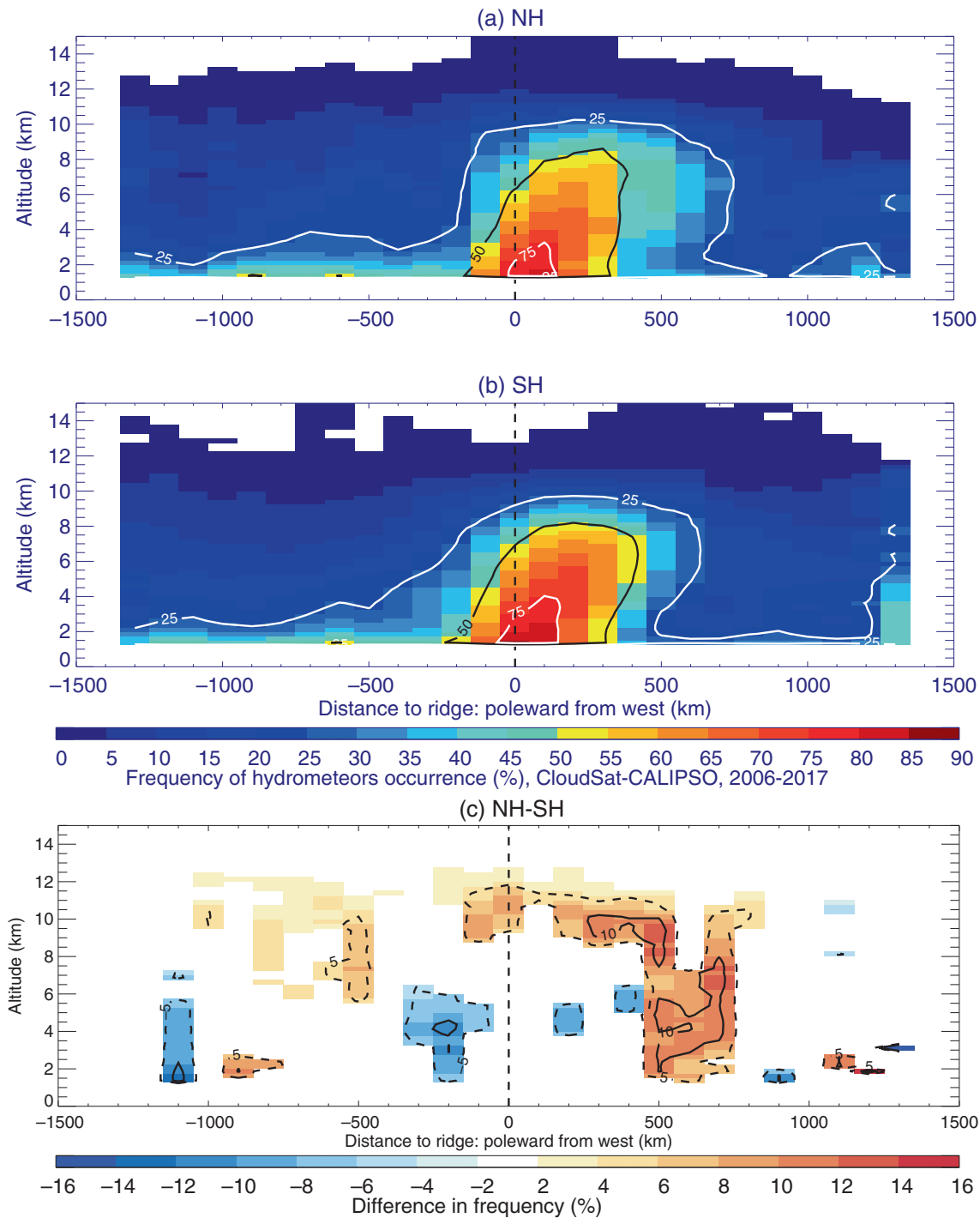


**FIGURE 12** Composite transects of hydrometeor frequency of occurrence across thermal ridges in (a) the Northern Hemisphere (NH) and (b) the Southern Hemisphere (SH), contoured in 5% increments from 0% to 90%; the solid contours highlight the 25%, 50%, and 75% levels. (c) Composite transect of the difference between NH and SH hydrometeor frequency of occurrence when exceeding the standard deviation across 100 difference transects obtained from a pair of 400 randomly selected thermal ridges. The dashed contours indicate the  $\pm 5\%$  difference level and the solid contours the  $\pm 10\%$  difference level. The vertical dashed line in all three panels indicates the location of the thermal ridge at 700 hPa.

and, third, the maximum in NH hydrometeor occurrence is less than that for the SH distribution (Figure 12b,c). Therefore SH OTR regions appear to be slightly shallower but cloudier than their NH counterparts. Note that the

differences between the two hemispheres are only shown where they exceed in absolute value one standard deviation of differences across a selection of 100 pairs of 400 randomly selected thermal ridges (selected independently

in the entire pool comprising both hemispheres and all seasons). Therefore the differences in hydrometeor frequencies between the two hemispheres are greater than the variability caused by non-uniform sampling.

For surface precipitation characteristics (Figure 13), the frequency of occurrence is fairly similar between the two hemispheres, but appears slightly shifted, with the SH peak in frequency found at the 700-hPa  $\theta_e$  ridge location, while at approx. 100 km poleward for NH (Figure 13a). Somewhat consistent with the contrast in hydrometeor distributions, the mean rain rates in the NH are noticeably larger than their SH counterparts (solid lines in Figure 13b). The median rain rate (dashed line in Figure 13b) in the NH is clearly less than the mean rate indicating the presence of some extraordinary precipitation events in the NH set of observations. Interestingly, the smaller difference between mean and median rates in the SH suggests a greater uniformity in precipitation intensity in SH occluded sectors. Also worthy of note is the fact that the NH median exceeds the SH median. Finally, radar attenuation occurs more often in the NH as well

(Figure 13c), consistent with the notion that precipitation in the vicinity of NH OTRs is heavy more frequently than it is in association with SH OTRs.

In order to better understand these several differences between the two hemispheres, the sensitivity of the cloud and precipitation distribution to other measurable characteristics of the thermal ridge is considered next.

## 5.2 | Sensitivity to $\theta_e$ by hemisphere

Figure 8 illustrated that the two hemispheres' occluded thermal ridges are characterized by different  $\theta_e$  distributions, with NH OTRs reaching much larger  $\theta_e$  values than their SH counterparts. A possible interpretation of the preceding analysis is that the drop in hydrometeor maximum frequency is tied to the relatively high  $\theta_e$  values predominantly found in the NH and not to some other physical difference between the hemispheres. In order to test this notion, we artificially impose a uniform distribution of  $\theta_e$  values in each hemisphere. This is accomplished

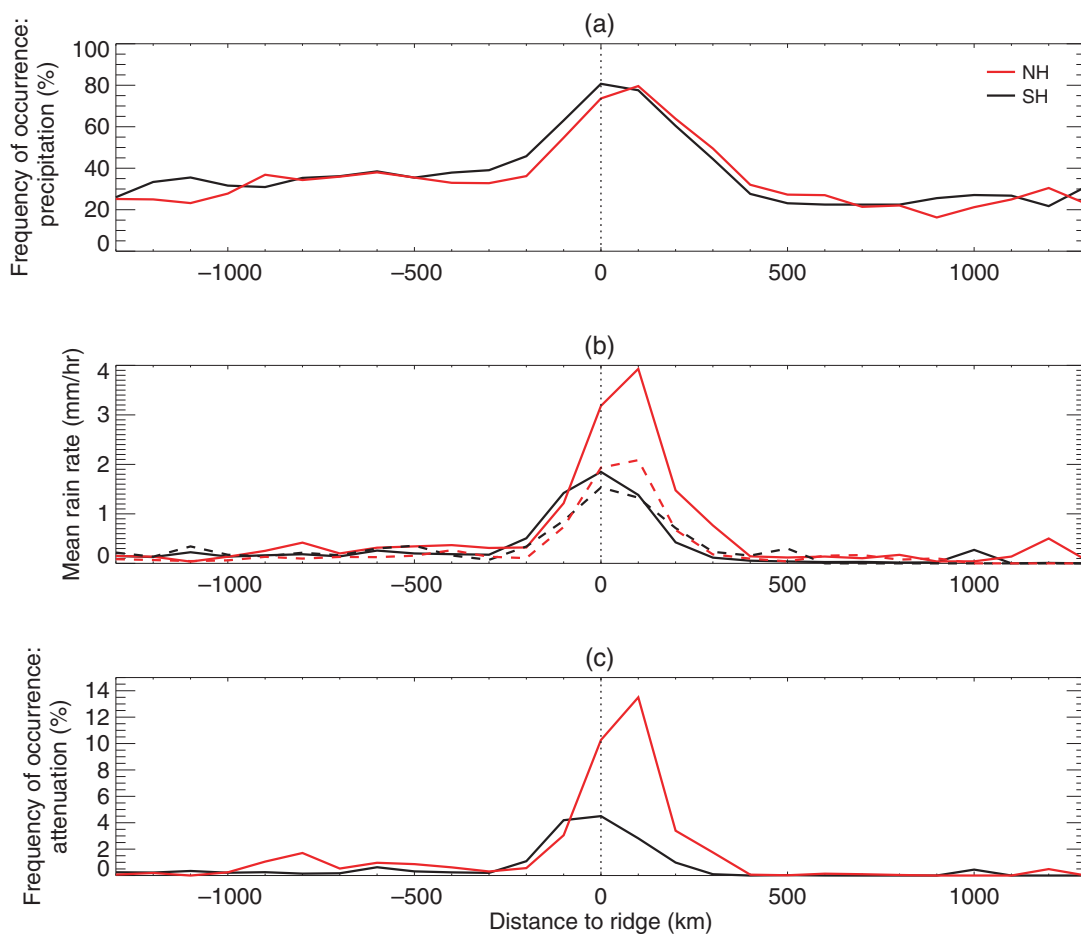


**FIGURE 13** Composite transect across all thermal ridges in the Northern Hemisphere (NH) (red) and Southern Hemisphere (SH) (black) of (a) the frequency of precipitation occurrence (%); (b) the mean (solid) and median (dashed) precipitation rate ( $\text{mm}\cdot\text{hr}^{-1}$ ); and (c) the frequency of occurrence of attenuation (%). The vertical dotted line in all three panels indicates the location of the thermal ridge at 700 hPa.

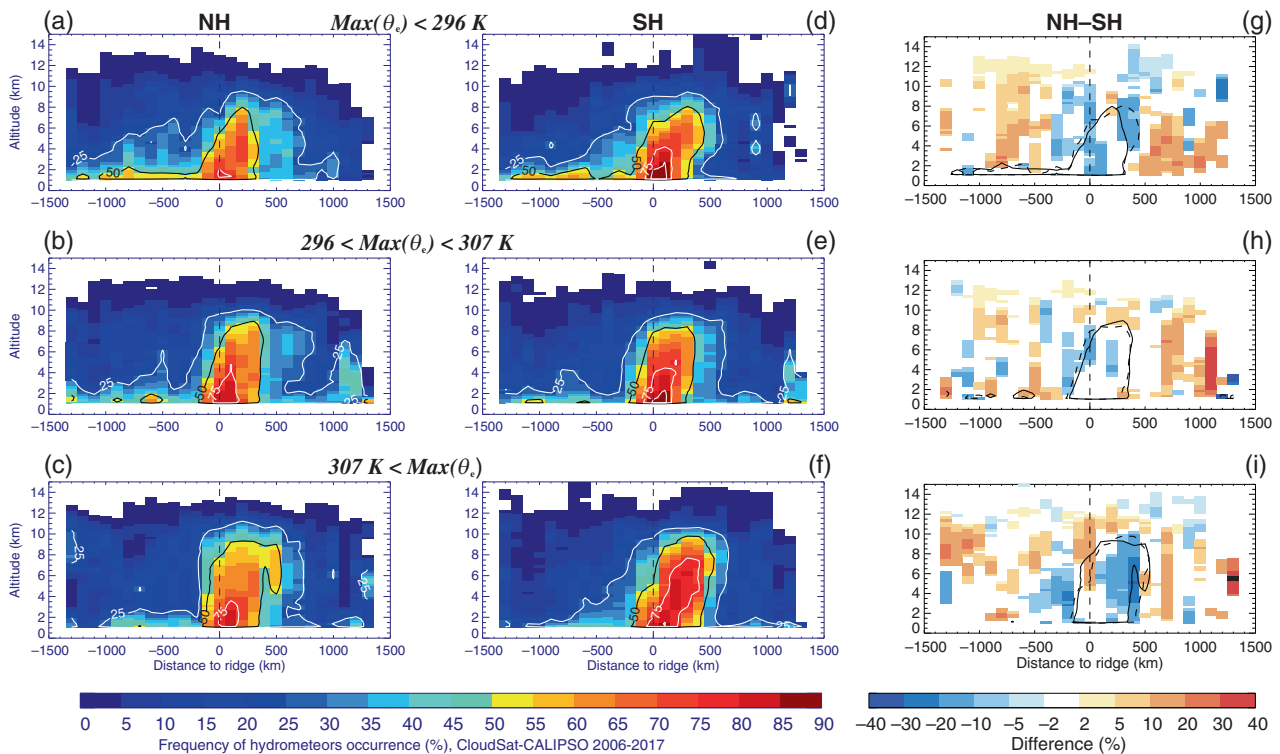


**FIGURE 14** Composite transects across thermal ridges in the (a, b, c) Northern (left column) and (d, e, f) Southern Hemisphere (SH) (middle column) of hydrometeor frequency of occurrence, in color (every 5% from 0% to 90%); and (g, h, i) of the difference between NH and SH frequency of hydrometeor occurrence where above — in absolute value — the standard deviation across a random selection of 100 pairs of 400 thermal ridges, for occluded thermal ridges (OTRs) classified based on the maximum value of  $\theta_e$ : (a, d, g)  $\max(\theta_e) < 296$  K; (b, e, h)  $296 < \max(\theta_e) < 307$  K; and (c, f, i)  $307 < \max(\theta_e)$ , with 25%, 50%, and 75% frequency level contours in (a–f), and 50% contour of NH (solid) and SH (dashed) frequencies in (g, h, i). The  $\max(\theta_e)$  categories are obtained using subsets of populations of both hemispheres forced to have the same  $\max(\theta_e)$  distribution, partitioned into three equal subsets of number of cases. The vertical dashed line indicates the location of the thermal ridge at 700 hPa.

by defining 1-K  $\theta_e$  bins spanning the entire range of  $\theta_e$  values in Figure 8. In each bin the number of identifications in each hemisphere is counted. If  $N$  is the lowest number between the two totals in a given  $\theta_e$  bin, we (1) use a random number generator to assign a number to each case in the larger set found in the other hemisphere, (2) use those random numbers to monotonically sort all the cases in that other hemisphere and (3) keep only the first  $N$  cases from that other hemisphere in that bin. In effect, in each hemisphere, the  $\theta_e$  distribution now follows the NH distribution from 240 to 301 K, then the SH distribution for  $\theta_e > 301$  K. The partitioning of the resulting truncated set of identifications produces three equal-size subsets with new thresholds of 296 and 307 K. The composite transects of hydrometeor frequency of occurrence in each hemisphere and in each  $\theta_e$  category are provided in Figure 14, along with the difference between the two hemispheres per category, and reveal the following: (1) for each  $\theta_e$  category, the maximum frequency of hydrometeor occurrence is larger in the SH than in the NH, but (2) clouds reach higher altitudes in the NH; (3) the warmest  $\theta_e$  category has a lower hydrometeor frequency maximum than

the cooler ones, in both hemispheres (cf. the 75% contour for NH and 85% for SH). Therefore, it appears that there is a  $\theta_e$  value above which the cloud and precipitation distributions behave differently, regardless of the hemisphere in which the occluded cyclone is located. Accordingly, the differences between the two hemispheres must depend on some other environmental factors.

## 6 | SUMMARY

Using 11 years of combined observations from CloudSat and CALIPSO, the distribution of cloud and precipitation across the occluded sectors of a large sample of extratropical cyclones is explored. The analysis relies on construction of composite profiles of hydrometeor occurrence along a transect line perpendicular to the OTR, anchored at the point of maximum 700-hPa  $\theta_e$  within the OTR. Consistent with the results of prior case studies (e.g., Crocker *et al.*, 1947; Godson, 1951; Martin, 1998a, 1998b; Penner, 1955), the maximum in cloud frequency and precipitation in the composites is found within the

area poleward of the thermal ridge, the TROWAL, and not at the surface-occluded front. Furthermore, frequencies of hydrometeor occurrence are close to saturation, in contrast with warm or cold frontal regions that display a lot more variability, within the frontal area as well as between fronts (Figure 4). In addition to higher hydrometeor frequencies in OTRs than warm frontal regions, it appears that while OTR's hydrometeor frequencies are sensitive to the cyclone-wide ascent strength, they show little sensitivity to environmental PW (Figure 6), in contrast with warm frontal regions (e.g., Field & Wood, 2007; Figure 7). It is possible that this disparity between OTRs and warm fronts is related to the nature of the ascent: warm frontal cloud and precipitation depend on frontogenetical forcing while the ascent in the occluded sector is fueled by a wave-scale forcing (Sutcliffe, 1947). Additionally, in this analysis only the condensate occurrence could be considered, not condensate amounts which might be more clearly dependent on PW.

As proposed in Naud *et al.* (2023), this analysis confirms that cloud and precipitation in OTRs are sensitive to the maximum in 700-hPa  $\theta_e$  in the ridge. The analysis reveals that there is a tendency for hydrometeor coverage to expand with increasingly higher  $\theta_e$  but there also appears to be a  $\theta_e$  threshold above which hydrometers maximum frequency drops, while precipitation rates increase. Though this is true in both hemispheres, the number of cases above this  $\theta_e$  “threshold” is relatively larger in the NH. These less frequent and more scattered hydrometeor distributions accompanied, as they are, by an uptick in precipitation intensity may be the signatures of a higher frequency of embedded convection in these environments. Such convection has been previously observed in or near the comma head of winter cyclones (Plummer *et al.*, 2015; Rauber *et al.*, 2015; Rosenow *et al.*, 2014), and in warm conveyor belts (Binder *et al.*, 2016; Binder *et al.*, 2020; Crespo & Posselt, 2016; Oertel *et al.*, 2019).

Overall, NH hydrometeor frequencies across the OTR are more horizontally extensive, deeper vertically and displaced farther poleward, than those in the SH, but the *maximum* in frequency is larger in the SH than in the NH. While precipitation in the vicinity of the OTR occurs with similar frequency in both hemispheres, NH precipitation rates are larger, mostly as a result of a larger number of cases with heavier than average precipitation. These differences are found even when forcing the distribution of maximum equivalent temperature in the ridge to be similar in the two hemispheres. While the differences between the two hemispheres are much smaller than those found between cyclones with different maximum  $\theta_e$ , the larger maximum in hydrometeor frequencies in the SH is intriguing and warrants further exploration. We hypothesize that this could be related to differences in static

stability, differences in the frequency of convection, or to differences in the ice and liquid content in clouds between the two hemispheres. We are currently exploring this latter possibility through analysis of ice and liquid water content profiles, also retrieved with CloudSat, and comparing composites made in both hemispheres. The hypothesis surrounding frequency of convection will be assessed in future work through use of Global Precipitation Measurement profiles of latent heating (GPM; Skofronick-Jackson *et al.*, 2017).

Finally, a similar analysis is being applied to output from the latest version of the Goddard Institute for Space Studies ESM (GISS Model E3; Cesana *et al.*, 2019). Preliminary results indicate that this model is capable of simulating the occlusion process with a realistic deep thermal and kinematic structure. However, occlusions tend to occur more frequently in the exit region of the storm tracks in the model than in the reanalysis. Therefore, using the CloudSat–CALIPSO transects discussed here as a benchmark, we will further scrutinize the model, to establish whether the representation of moist processes in the model, or a broader large-scale circulation difference, plays a role in the occlusion frequency issue. This will constitute a novel way of evaluating climate models and promises to provide new insight on both large-scale and process-level performance.

## ACKNOWLEDGEMENTS

A portion of this work was conducted at the Jet Propulsion Laboratory, California Institute of Technology, under a contract with the National Aeronautics and Space Administration (80NM0018D0004). The work is funded by NASA's CloudSat–CALIPSO Science Team program grant 80NSSC20K0085. We thank two anonymous reviewers for their insightful comments that helped improve this manuscript.

## DATA AVAILABILITY STATEMENT

The database of occluded cyclones and the database of cyclones with cold and warm front identifications are described and accessible here: <https://data.giss.nasa.gov/storms/obs-etc/>. CloudSat–CALIPSO 2B–GEOPROF–LIDAR and 2C–PRECIP–COLUMN data files are documented and available here: <https://www.cloudsat.cira.colostate.edu/>. MERRA2 precipitable water and vertical velocity information are available in these files: Global Modeling and Assimilation Office (GMAO) (2015), MERRA-2 tavg1\_2d\_slv\_Nx: 2d, 1-Hourly, Time-Averaged, Single-Level, Assimilation, Single-Level Diagnostics V5.12.4, Greenbelt, MD, USA, Goddard Earth Sciences Data and Information Services Center (GES DISC), Accessed: 2020-01, 10.5067/VJAFPLI1CSIV. Moderate Resolution Imaging

spectroradiometer (MODIS) daily mosaics of visible images are available through NASA's EOSDIS worldview application: <https://worldview.earthdata.nasa.gov/>.

## ORCID

Catherine M. Naud  <https://orcid.org/0000-0002-3914-1498>

Poushali Ghosh  <https://orcid.org/0000-0002-3319-0416>

Jonathan E. Martin  <https://orcid.org/0000-0003-3992-8458>

Gregory S. Elsaesser  <https://orcid.org/0000-0001-5785-4451>

Derek J. Posselt  <https://orcid.org/0000-0002-5670-5822>

## REFERENCES

- Binder, H., Boettcher, M., Joos, H. & And Wernli, H. (2016) The role of warm conveyor belts for the intensification of extratropical cyclones in northern hemisphere winter. *Journal of the Atmospheric Sciences*, 73, 3997–4020.
- Binder, H., Boettcher, M., Joos, H., Sprenger, M. & Wernli, H. (2020) Vertical cloud structure of warm conveyor belts—a comparison and evaluation of ERA5 reanalysis, CloudSat and CALIPSO data. *Weather and Climate Dynamics*, 1, 577–595. Available from: <https://doi.org/10.5194/wcd-1-577-2020>
- Bjerknes, J. & Solberg, H. (1922) Life cycle of cyclones and the polar front theory of atmospheric circulation. *Geophysisks Publikationer*, 3(1), 1–18.
- Booth, J.F., Naud, C.M. & Del Genio, A.D. (2013) Diagnosing warm frontal cloud formation in a GCM: A novel approach using conditional subsetting. *Journal of Climate*, 26, 5827–5845.
- Cesana, G., Del Genio, A.D., Ackerman, A.S., Kelley, M., Elsaesser, G., Fridlind, A.M. et al. (2019) Evaluating models' response of tropical low clouds to SST forcings using CALIPSO observations. *Atmospheric Chemistry and Physics*, 19, 2813–2832. Available from: <https://doi.org/10.5194/acp-19-2813-2019>
- Crespo, J.A. & Posselt, D.J. (2016) A-train-based case study of stratiform-convective transition within a warm conveyor belt. *Monthly Weather Review*, 144, 2069–2084. Available from: <https://doi.org/10.1175/MWR-D-15-0435.1>
- Crocker, A., Godson, W.L. & Penner, C.M. (1947) Frontal contour charts. *Journal of the Atmospheric Sciences*, 4(3), 95–99.
- Field, P.R. & Wood, R. (2007) Precipitation and cloud structure in midlatitude cyclones. *Journal of Climate*, 20, 233–254. Available from: <https://doi.org/10.1175/JCLI3998.1>
- Gelaro, R., McCarty, W., Suarez, M.J., Todling, R., Molod, A., Takacs, L. et al. (2017) The modern-era retrospective analysis for research and applications, version 2 (MERRA-2). *Journal of Climate*, 30(14), 5419–5454.
- Godson, W.L. (1951) Synoptic properties of frontal surfaces. *Quarterly Journal of the Royal Meteorological Society*, 77(334), 633–653.
- Govekar, P.D., Jakob, C. & Catto, J. (2014) The relationship between clouds and dynamics in southern hemisphere extratropical cyclones in the real world and a climate model. *Journal of Geophysical Research*, 119, 6609–6628. Available from: <https://doi.org/10.1002/2013JD020699>
- Grim, J.A., Rauber, R.M., Ramamurthy, M.K., Jewett, B.F. & Han, M. (2007) High-resolution observations of the Trowal-warm-frontal region of two continental winter cyclones. *Monthly Weather Review*, 135, 1629–1646. Available from: <https://doi.org/10.1175/MWR3378.1>
- Han, M., Rauber, R.M., Ramamurthy, M.K., Jewett, B.F. & Grim, J.A. (2007) Mesoscale dynamics of the TROWAL and warm-frontal regions of two continental winter cyclones. *Monthly Weather Review*, 135, 1647–1670. Available from: <https://doi.org/10.1175/MWR3377.1>
- Hawcroft, M.K., Shaffrey, L.C., Hodges, K.I. & Dacre, H.F. (2012) How much northern hemisphere precipitation is associated with extratropical cyclones? *Geophysical Research Letters*, 39, L24809. Available from: <https://doi.org/10.1029/2012GL053866>
- Haynes, J.M., L'Ecuyer, T.S., Stephens, G.L., Miller, S.D., Mitrescu, C., Wood, N.B. et al. (2009) Rainfall retrieval over the ocean with spaceborne W-band radar. *Journal of Geophysical Research*, 114, D00A22. Available from: <https://doi.org/10.1029/2008JD009973>
- Hewson, T.D. (1998) Objective fronts. *Meteorological Applications*, 5(1), 37–65.
- Lackmann, G.M. (2002) Cold-frontal potential vorticity maxima, the low-level jet, and moisture transport in extratropical cyclones. *Monthly Weather Review*, 130(1), 59–74. Available from: [https://doi.org/10.1175/1520-0493\(2002\)130<0059:CFPVMT>2.0.CO;2](https://doi.org/10.1175/1520-0493(2002)130<0059:CFPVMT>2.0.CO;2)
- Mace, G.G. & Zhang, Q. (2014) The CloudSat radar-lidar geometrical profile product (RL-GeoProf): Updates, improvements, and selected results. *Journal of Geophysical Research – Atmospheres*, 119, 9441–9462. Available from: <https://doi.org/10.1002/2013JD021374>
- Mace, G.G., Zhang, Q., Vaughan, M., Marchand, R., Stephens, G., Trepte, C. et al. (2009) A description of hydrometeor layer occurrence statistics derived from the first year of merged CloudSat and CALIPSO data. *Journal of Geophysical Research*, 114, D00A26. Available from: <https://doi.org/10.1029/2007JD008755>
- Marchand, R., Mace, G.G., Ackerman, T. & Stephens, G. (2008) Hydrometeor detection using *CloudSat*—an earth-orbiting 94-GHz cloud radar. *Journal of Atmospheric and Oceanic Technology*, 25, 519–533.
- Marciano, C.G., Lackmann, G.M. & Robinson, W.A. (2015) Changes in U.S. east coast cyclone dynamics with climate change. *Journal of Climate*, 28, 468–484. Available from: <https://doi.org/10.1175/JCLI-D-14-00418.1>
- Martin, J.E. (1998a) The structure and evolution of a continental winter cyclone. Part I: Frontal structure and the occlusion process. *Monthly Weather Review*, 126(2), 303–328.
- Martin, J.E. (1998b) The structure and evolution of a continental winter cyclone. Part II: Frontal forcing of an extreme snow event. *Monthly Weather Review*, 126(2), 329–348.
- Martin, J.E. (1999a) Quasi-geostrophic forcing of ascent in the occluded sector of cyclones and the trowal airstream. *Monthly Weather Review*, 127, 70–88.
- Martin, J.E. (1999b) The separate roles of geostrophic vorticity and deformation in the mid-latitude occlusion process. *Monthly Weather Review*, 127, 2404–2418.
- Martin, J.E. (2006) *Mid-Latitude Atmospheric Dynamics: A First Course*. West Sussex, England: John Wiley Sons, Ltd.
- Michaelis, A.C., Willison, J., Lackmann, G.M. & Robinson, W.A. (2017) Changes in winter North Atlantic extratropical cyclones in high-resolution regional pseudo-global warming simulations. *Journal of Climate*, 30, 6905–6925. Available from: <https://doi.org/10.1175/JCLI-D-16-0697.1>
- Naud, C.M., Booth, J.F. & Del Genio, A.D. (2016) The relationship between boundary layer stability and cloud cover in the post-cold

- frontal region. *Journal of Climate*, 29(22), 8129–8149. Available from: <https://doi.org/10.1175/JCLI-D-15-0700.1>
- Naud, C.M., Booth, J.F., Lebsock, M. & Grecu, M. (2018) Observational constraint for precipitation in extratropical cyclones: Sensitivity to data sources. *Journal of Applied Meteorology and Climatology*, 57(4), 991–1009. Available from: <https://doi.org/10.1175/JAMC-D-17-0289.1>
- Naud, C.M., Del Genio, A.D., Bauer, M. & Kovari, W. (2010) Cloud vertical distribution across warm and cold fronts in CloudSat–CALIPSO data and a general circulation model. *Journal of Climate*, 23, 3397–3415. Available from: <https://doi.org/10.1175/2010JCLI3282.1>
- Naud, C.M., Martin, J.E., Ghosh, P., Elsaesser, G.S. & Posselt, D.J. (2023) Automated identification of occluded sectors in mid-latitude cyclones: Method and some climatological applications. *Quarterly Journal of the Royal Meteorological Society*, 149, 1990–2010. Available from: <https://doi.org/10.1002/qj.4491>
- Naud, C.M., Posselt, D.J. & van den Heever, S.C. (2018) Reply to comments on ‘A CloudSat–CALIPSO view of cloud and precipitation properties across cold fronts over the global oceans’. *Journal of Climate*, 31(7), 2969–2975. Available from: <https://doi.org/10.1175/JCLI-D-17-0777.1>
- Naud, C.M., Posselt, D.J. & van den Heever, S.C. (2012) Observational analysis of cloud and precipitation in midlatitude cyclones: Northern versus southern hemisphere warm fronts. *Journal of Climate*, 25, 5135–5151. Available from: <https://doi.org/10.1175/JCLI-D-11-00569.1>
- Naud, C.M., Posselt, D.J. & van den Heever, S.C. (2015) A CloudSat–CALIPSO view of cloud and precipitation properties across cold fronts over the global oceans. *Journal of Climate*, 28(17), 6743–6762. Available from: <https://doi.org/10.1175/JCLI-D-15-0052.1>
- Naud, C.M., Posselt, D.J. & van den Heever, S.C. (2017) Observed covariations of aerosol optical depth and cloud cover in extratropical cyclones. *Journal of Geophysical Research – Atmospheres*, 122(19), 10338–10356. Available from: <https://doi.org/10.1002/2017JD027240>
- Oertel, A., Boettcher, M., Joos, H., Sprenger, M., Konow, H., Hagen, M. et al. (2019) Convective activity in an extratropical cyclone and its warm conveyor belt – a case-study combining observations and a convection-permitting model simulation. *Quarterly Journal of the Royal Meteorological Society*, 145, 1406–1426. Available from: <https://doi.org/10.1002/qj.3500>
- Penner, C. (1955) A three-front model for synoptic analyses. *Quarterly Journal of the Royal Meteorological Society*, 81(347), 89–91.
- Plummer, D.M., McFarquhar, G.M., Rauber, R.M., Jewett, B.F. & Leon, D.C. (2015) Microphysical properties of convectively generated fall streaks within the stratiform comma head region of continental winter cyclones. *Journal of the Atmospheric Sciences*, 72, 2465–2483.
- Posselt, D.J. & Martin, J.E. (2004) The effect of latent heat release on the evolution of a warm occluded thermal structure. *Monthly Weather Review*, 132, 578–599.
- Rauber, R.M.D.M., Plummer, M.K., Macomber, A.A., Rosenow, G.M., McFarquhar, B.F., Jewett, D. et al. (2015) The role of cloud-top generating cells and boundary layer circulations in the Finescale radar structure of a winter cyclone over the Great Lakes. *Monthly Weather Review*, 143, 2291–2318.
- Rosenow, A.A., Plummer, D.M., Rauber, R.M., McFarquhar, G.M., Jewett, B.F. & Leon, D. (2014) Vertical velocity and physical structure of generating cells and convection in the comma head region of continental winter cyclones. *Journal of the Atmospheric Sciences*, 71, 1538–1558.
- Schultz, D.M. (2018) Comments on “a CloudSat–CALIPSO view of cloud and precipitation properties across cold fronts over the global oceans”. *Journal of Climate*, 31, 2965–2967. Available from: <https://doi.org/10.1175/JCLI-D-17-0619.1>
- Schultz, D.M. & Vaughan, G. (2011) Occluded fronts and the occlusion process: A fresh look at conventional wisdom. *Bulletin of the American Meteorological Society*, 92(4), 443–466.
- Simmonds, I., Keay, K. & Tristram Bye, J.A. (2012) Identification and climatology of southern hemisphere mobile fronts in a modern reanalysis. *Journal of Climate*, 25(6), 1945–1962.
- Skofronick-Jackson, G., Petersen, W.A., Berg, W., Kidd, C., Stocker, E.F., Kirschbaum, D.B. et al. (2017) The global precipitation measurement (GPM) mission for science and society. *Bulletin of the American Meteorological Society*, 98, 1679–1695. Available from: <https://doi.org/10.1175/BAMS-D-15-00306.1>
- Stephens, G.L., Vane, D.G., Boain, R.J., Mace, G.G., Sassen, K., Wang, Z. et al. (2002) The CloudSat mission and the A-TRAIN: A new dimension to space-based observations of clouds and precipitation. *Bulletin of the American Meteorological Society*, 83, 1771–1790.
- Stephens, G.L., Vane, D.G., Tanelli, S., Im, E., Durden, S., Rokey, M. et al. (2008) CloudSat mission: Performance and early science after the first year of operation. *Journal of Geophysical Research*, 113, D00A18. Available from: <https://doi.org/10.1029/2008JD009982>
- Sutcliffe, R. (1947) A contribution to the problem of development. *Quarterly Journal of the Royal Meteorological Society*, 73(317–318), 370–383.
- Sutcliffe, R.C. & Forsdyke, A.G. (1950) The theory and use of upper air thickness patterns in forecasting. *Quarterly Journal of the Royal Meteorological Society*, 76(328), 189–217. Available from: <https://doi.org/10.1002/qj.49707632809>
- Uccellini, L.W. (1990) Processes contributing to the rapid development of extratropical cyclones. In: Newton, C.W. & Holopainen, E.O. (Eds.) *Extratropical cyclones: the Erik Palmén memorial volume*. American Meteorological Society, Boston, MA. pp. 81–105.
- Winker, D.M., Vaughan, M.A., Omar, A.H., Hu, Y., Powell, K.A., Liu, Z. et al. (2009) Overview of the CALIPSO Mission and CALIOP data processing algorithms. *Journal of Atmospheric and Oceanic Technology*, 26, 2310–2323.
- Zhang, Z. & Colle, B.A. (2017) Changes in extratropical cyclone precipitation and associated processes during the twenty-first century over eastern North America and the Western Atlantic using a cyclone-relative approach. *Journal of Climate*, 30, 8633–8656. Available from: <https://doi.org/10.1175/JCLI-D-16-0906.1>

**How to cite this article:** Naud, C.M., Ghosh, P., Martin, J.E., Elsaesser, G.S. & Posselt, D.J. (2024) A CloudSat–CALIPSO view of cloud and precipitation in the occluded quadrants of extratropical cyclones. *Quarterly Journal of the Royal Meteorological Society*, 150(760), 1336–1356. Available from: <https://doi.org/10.1002/qj.4648>